ADVANCED MATERIALS INTERFACES
Open Access
www.advmatinterfaces.de

A Review on Reactor Design and Surface Modification of Atomic Layer Deposition for Functional Nanoparticles

Guanghui Yan, Gaoshan Huang, Jianjun Shi, Yi Ouyang, Xueqin Zuo, Zhihao Bao, and Yongfeng Mei**

Atomic layer deposition (ALD) has emerged as a promising method for surface modification of functional nanoparticles, enabling the versatile applications in energy, catalysis, and human health. The self-limiting surface chemistry of ALD allows not only the coating of ultrathin and conformal films but also the decoration of nanoparticle surfaces with specific nanoclusters under appropriate processing conditions. In particle ALD, one of the major challenges lies in the strong cohesive force causing nanoparticle agglomerates or aggregates, which requires their homogeneous dispersion. This review provides an overview on the developments and advancements of particle ALD, covering both reactor designs and applications. The fundamentals of ALD are first reviewed, followed by the reactor designs including fluidized bed reactors, rotating bed reactors, and atmospheric-pressure continuous spatial ALD reactors. Among them, the basics of particle fluidization are concisely outlined to establish a foundation for understanding fluidized bed reactors. The advantages and disadvantages of various reactor designs are compared and analyzed. Subsequently, the applications of ALD-modified nanoparticles are reviewed, with a focus on energy, catalysis, biomedicine, and cosmetics. Finally, the progress and applications of ALD modification for functional nanoparticles are summarized, and the perspectives in the field are proposed.

1. Introduction

Ultrafine particles, especially nanoparticles (NPs) with a size below 100 nm, have attracted much attention both in scientific community and industrial sectors.[1,2] Due to the small primary particle size and large surface area-to-volume ratio, this kind of particles may exhibit new chemical, physical, and biological properties, resulting in great potential in the applications of energy,[3] catalysis,[4,5] pharmaceuticals,[6,7] cosmetics,[8–10] and sensing.[11] To achieve the potential uses in the emerging application fields, surface modification of NPs have aroused growing interest,[12–16] even though the synthesis method is still of importance for NPs.[17–19] To modify the surface properties while maintaining the bulk properties, a conformal and ultrathin film on NPs is crucial. On the other hand, NPs occasionally need specific surface decorations, like nanoclusters, for unique functionality.[4,20,21] To this end, it calls for a technology which has the ability not only in providing conformal and ultrathin coatings on complex structures, but also in decorating specific nanoclusters on NP surfaces. Over the past decades, atomic layer deposition (ALD), a gas–solid surface reaction technique, has been already explored to deposit films on varying substrates, such as flat substrates, nanowires, carbon nanotubes, porous materials, etc., to enhance the functionality of materials.[13,14,16] ALD shows the ability in modifying the particles with encapsulation layers, passivation layers, barrier layers, and surface-reactive catalysts.[13,16] Furthermore, ALD can deposit many materials onto the particle substrates, including metal oxides, metal nitrides, metal sulfides, noble metals, and others.[22–24] Therefore, ALD has been regarded as a promising tool for surface modification due to its virtues of conformality and sub-nanometer thickness control as well as nanocluster deposition.[13,14,16]

G. Yan, G. Huang, J. Shi, Y. Ouyang, Z. Bao, Y. Mei
Yiwu Research Institute of Fudan University
Yiwu City, Zhejiang 322000, P. R. China
E-mail: yangh@ywfudan.cn; yfm@fudan.edu.cn

The ORCID identification number(s) for the author(s) of this article can be found under https://doi.org/10.1002/admi.202500140

DOI: 10.1002/admi.202500140

G. Huang, X. Zuo, Y. Mei
Department of Materials Science and State Key Laboratory of Molecular Engineering of Polymers
Fudan University
Shanghai 200438, P. R. China

G. Huang, Y. Mei
International Institute of Intelligent Nanorobots and Nanosystems
Fudan University
Shanghai 200438, P. R. China

Y. Mei
Shanghai Frontiers Science Research Base of Intelligent Optoelectronics and Perception
Institute of Optoelectronics
Fudan University
Shanghai 200438, P. R. China

Although ALD technology has emerged as a promising method for surface modification, some challenges still exist in the modification of (nano)particles. Compared to the flat substrates, the processing conditions for NPs may distinctly differ from their planar counterparts due to the high aspect ratio and irregular shapes of NPs. Moreover, NPs usually exhibit strong interparticle forces and thereby individual particles tend to attract each other to form agglomerates or aggregates,[25] which may result in nonuniform coating or uncoated area. In this respect, one of the foremost challenges is homogeneous dispersion of NPs in gaseous media for total coverage of the reactants. To obtain the dispersion of NPs, appropriate reactors have to be designed for particle ALD (PALD). In 2014, Longrie et al. presented a brief review on the reactor designs of PALD.[26] In 2019, Dr. Weimer, an expert in the ALD field, presented an excellent review about PALD,[16] which is very helpful to understand the PALD knowledge for the readership. At the same year, van Ommen et al. also provided a compact review on PALD with briefly reviewing on reactor, applications, potential scale-up, etc.[13] After the year of 2019, there are some new developments of PALD both in reactor designs and applications, such as atmospheric-pressure ALD. Thus, to promote the development of this field, it is necessary to timely summarize the recent progress of PALD.

In comparison to other reviews, this review will provide an overview on the development and advancement of temporal ALD (t-ALD) reactors used in PALD, from static bed reactors to fluidized bed reactors (FBRs), rotating bed reactors and vibrating bed reactors. Since the large quantity of particles needs to be processed in the practical applications which requires scale-up solutions for PALD, this paper will discuss the application of atmospheric-pressure spatial ALD (s-ALD) in the particle modification, focusing on high-throughput methods such as batch processing and continuous processing. The advantages and disadvantages between different reactor designs are compared and analyzed. After that, the applications of ALD-modified NPs in the fields of energy, catalysis, bio-medicine, cosmetics and ceramics will be discussed by highlighting the current literature. Finally, we conclude the progress of ALD modification technique for functional NPs and put forward our perspectives in this field.

2. Fundamentals of ALD

ALD is a derivation from chemical vapor deposition (CVD) and has its unique characteristics. One of the main differences between ALD and CVD lies in the method of introducing reactants into the reactor. In CVD process, the gaseous reactants are simultaneously introduced into the reactor, resulting in both gas and surface reactions on the substrate.[27] However, in a typical ALD process, gaseous reactants are sequentially pulsed into the reactor and react with finite surface sites on the substrate surfaces, and intermediately purging steps are carried out between reactant pulses to pump out the excessive reactants and reaction byproducts.[24] Thanks to the special introduction of reactants, ALD can offer a dense and pinhole-free film with precise thickness control on high aspect ratio structures including NPs.[24,28] To obtain the desired film deposited via ALD, the surface chemical properties of substrates and process conditions should be taken into account seriously. Thus, this section will give a brief introduction to the fundamentals of ALD, including the concept of film deposition, the surface chemistry and processing conditions associated with ALD reactions.

2.1. Concept of Thin Film Deposition by ALD

Typically, one ALD reaction cycle can be divided into four steps,[23,29] as shown in **Figure 1**. Specifically, the full steps of ALD process are as follows:

Step 1: dosing the reactant A pulse for a complete chemisorption on the substrate;
Step 2: purging the excessive reactant A with the inert gas;
Step 3: dosing the reactant B pulse for a complete reaction with the reactant A;
Step 4: purging the by-products and excessive reactant B with the inert gas.

In the first step, the surface of the substrate is exposed to the molecules of reactant A and allows the chemisorption of reactant molecules onto the active surface sites. After that, the excessive molecules of reactant A are purged by the inert gas in the second step. In the third step, the reactant B is introduced to undergo a reaction with the adsorbed reactant A molecules and form a solid product onto the substrate surfaces. The fourth step involves the removal of excessive reactant B molecules and the by-products generated by the third step. The process of reactant pulses and purging steps constitute one ALD cycle that determines the thickness of the deposited film. The growth rate denoted as growth per cycle (GPC) can be simply and precisely controlled by repeating the number of ALD reaction cycles. Normally, the final film deposited by ALD is amorphous or poly-crystalline. In a typical ALD process, the purging steps, which divide the ALD reactions into two half-reactions, play a significant role in preventing the coexistence of reactant A and B. If reactant A and reactant B coexist in the chamber, the CVD reaction may happen, thereby giving rise to an abnormal film growth.

With the unique reaction fashion, the major advantages of depositing films by ALD are in that:[12,13] 1) the film thickness with Angstrom level can be simply controlled by the number of ALD cycles, as the thickness is proportional to the number of reaction cycles under the assumption that there is no nucleation delay of film growth in the beginning of ALD cycles and the newly deposited film surface do not affect the successive film growth; 2) it can be used to deposit large-area films with excellent conformality and homogeneity via the use of chemisorbed reactants. The coating films with controlled thickness and conformality allow that the ALD process has the potential use in the modification of micro/nanoparticles.

The above-mentioned conventional ALD process with the pulses of reactants being intermitted by purging steps is also deemed as t-ALD process (**Figure 2a**).[30] It is reported that the purging step takes up at least 50% of the total process time of a standard ALD process.[31] Thus, the low deposition rate is one of the major drawbacks of the t-ALD process. To eliminate the purging steps, the s-ALD process has been proposed (Figure 2b).[30] In the s-ALD process, the reactants are simultaneously fed into the different locations of the reactor separated by an inert gas zone, while the substrate can move to the different reactant zones to fulfill the half-reactions. With developing a kinetic model of s-ALD,

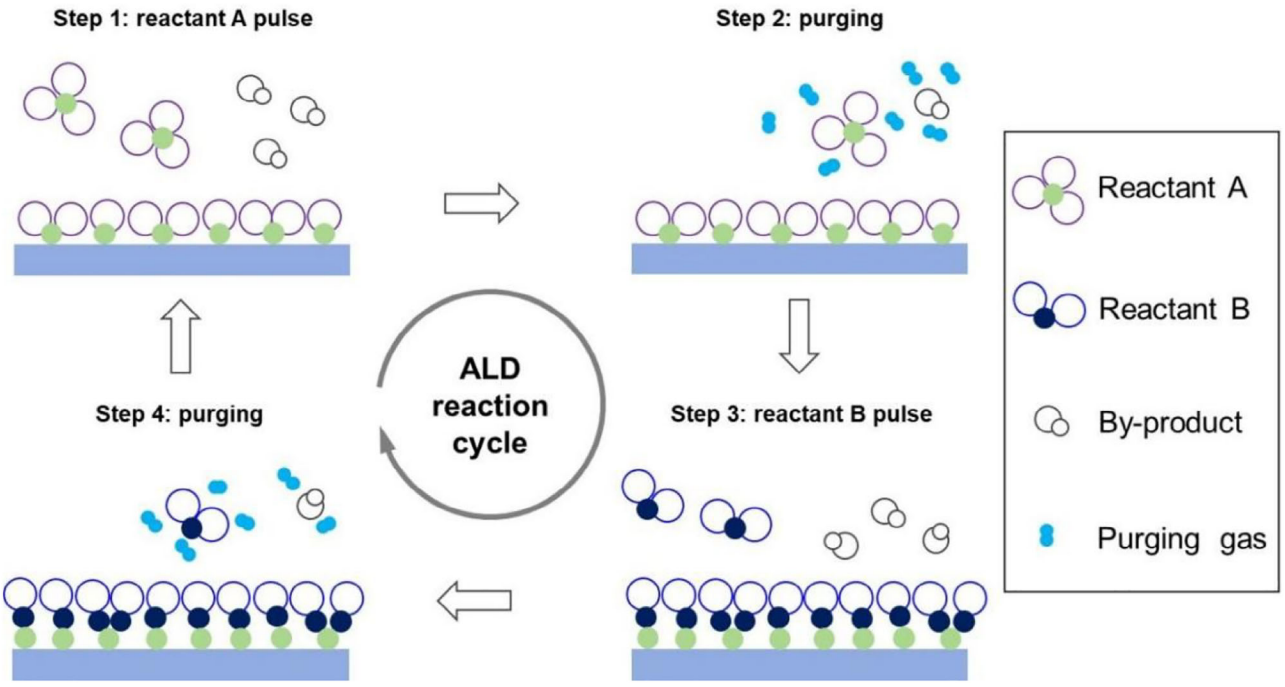

Figure 1. Schematic of the sequential ALD cycle. Step 1: Pulse of reactant A and its absorption on the surface. Step 2: Pulse of purging gas and removal of the unabsorbed reactant A. Step 3: Pulse of reactant B and reaction between reactant A and reactant B on the substrate surface. Step 4: Pulse of purging gas and removal of the byproduct generated by reaction of reactant A and reactant B, and the unreacted reactant B. Reproduced with permission.[24] Copyright 2010, American Chemical Society.

Poodt et al.[32] estimated that the maximum alumina deposition rate can reach several nm/s, showing drastic enhancement of the deposition rate. Consequently, s-ALD has attracted much attention from the scientific and engineering community.[30,33]

2.2. Surface Characteristics and Processing Conditions

ALD is a self-limiting surface reaction which is due to the irreversible chemisorption of reactant species on the substrate surfaces. The properties of substrates, especially the surface species, have significant influence on the ALD surface reactions. Taking Al_2O_3 ALD with trimethylaluminium (TMA) and H_2O as an example, the sequential A-B half reactions can be expressed as the following equations:[23,24]

$$AlOH^{*}+Al(CH_3)_3\,(g) \rightarrow AlOAl(CH_3)_2{}^{*}+CH_4\,(g) \quad (1)$$

$$AlCH_3{}^{*} + H_2O\,(g) \rightarrow AlOH^{*}+CH_4\,(g) \quad (2)$$

where the asterisks denote the surface species. In the half-reaction A, the substrate surfaces with hydroxyl species are exposed to undergo reactions with TMA molecules and switch to methyl species completely. In the half-reaction B, the methyl-terminated surfaces change to hydroxyl-terminated surfaces. According to the above A-B equations, it indicates that the hydroxyl species on the substrate surfaces facilitate the onset of the formation of alumina film. Therefore, the substrates can be treated to promote the ALD surface reaction, and the treatment of substrates depends on the materials to be deposited and ALD reactions.[34] Through the sequential A-B reactions, Al_2O_3 film is deposited with the film thickness controlled by the number of ALD cycles. Previously, the ALD process is deemed as a monolayer deposition technology. Actually, the description of monolayer deposition in ALD is not appropriate in nature. Because of the steric hindrance effect of ligands and density of reactive surface sites on the substrate surface,[35] the GPC in ALD is indeed less than one monolayer, usually less than 50% monolayer as reported in the previous literature.[36,37] The GPC is also affected by the growth modes. In ALD, there may exist three types of growth modes, namely, (a) two-dimensional growth, (b) island growth, and (c) random growth,[35] as illustrated in **Figure 3**. The two-dimensional growth is an ideal growth mode because that the reactant molecules are chemically absorbed on the substrate surfaces via the manner of monolayer. If the reactant vapors are inactive on the substrate surfaces, the film growth prefers to take place selectively in the reactive area of the surfaces, such as defects area on the substrate surfaces, resulting in island growth mode. It was reported that the growth mode of ZrO_2 and Al_2O_3 on hydrogen-terminated surface belongs to island growth.[38] The random growth mode refers to the film growth that the materials to be deposited are distributed on the substrates randomly. It should be noted that the configuration of reactors and properties of the substrate surfaces play important influence on the growth mode. At the beginning of the film growth, the film usually experiences nucleation. A nucleation retardation phenomenon is observed in the beginning of film formation in the ALD process.[38] It implies that controlling the initial growth of the materials to be deposited in ALD can be used to grow nanoclusters to decorate the designated catalysts.[4,21]

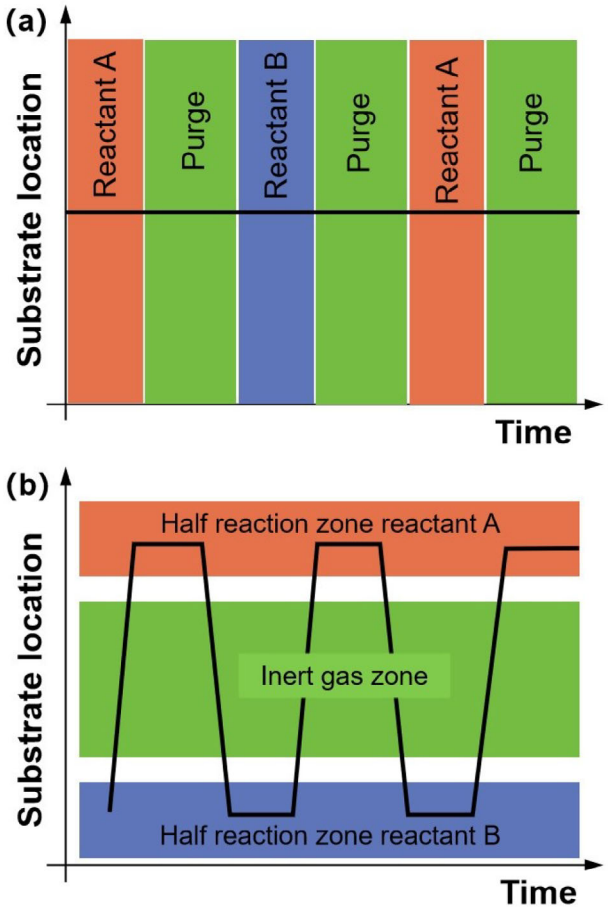

Figure 2. a,b) Schematic diagrams of t-ALD and s-ALD. Reproduced with permission.[30] Copyright 2012, American Vacuum Society.

In ALD, the processing conditions, such as temperature, pressure, and time, are needed to be tuned appropriately to achieve an ideal deposition. Temperature is an important parameter in the ALD surface reactions because that it can provide the appropriate activation energy for the chemisorption and related reactions in ALD. The ALD reaction can only proceed in a confined zone of temperature, named as "temperature window" (**Figure 4**), which was first found by Suntola et al. in 1980.[22] At higher temperatures, the chemical desorption rate becomes low. However, the decomposition of reactant vapors and surface species may take place, resulting in additional reactions and film growth. At low temperatures, the reactant vapors may condense on the substrate surfaces and the surface reactions may not reach completion due to the lack of enough energy. Thus, to achieve an ideal deposition behavior, it is recommended to carry out the ALD process in the appropriate temperature range.[39]

Normally, the ALD surface reaction is considered to be thermodynamically favorable. And the chemisorption of reactant vapors on the substrate surfaces is fast kinetics.[35] However, the fast kinetics of chemisorption is followed by a series of slow reactions consisting of the removal of excessive reactants and reaction byproducts, and surface diffusion. Thus, the exposure and purging times also affect the ALD film growth. For particles and porous substrates, the reactants require long exposure to facilitate sufficient diffusion into the substrate surfaces. It was reported that Al_2O_3 growth on the flat substrates only requires exposure time of milliseconds to deposit a conformal monolayer,[40] while it takes about one minute to deposit a conformal film for high-aspect-ratio structures with the pore depth of 50 μm and diameter of 65 nm.[24,28] It indicates that sufficient exposure time and purging time are needed when using ALD to modify the surfaces of particles.

The operating pressure is considered to influence the course of mass transfer and thereby affects the film growth in ALD. The absolute pressure in the ALD process is the sum of partial pressures of reactant, byproduct and carrier gas. Due to the thermodynamic nature of chemisorption in the ALD surface reaction, the partial pressure of the reactant has negligible effect on the surface chemistry. However, the weak gas–solid interactions induced by low pressure can affect the ALD film growth. Under the assumption of stepwise reactive sticking coefficient, Gordon et al. deduced a formula to estimate the partial pressure (P) and exposure time (t) for complete coating of the sidewalls of high-aspect-ratio (a) structures per cycle, which was expressed as following:[40]

$$P \cdot t = S\sqrt{2\pi mkT}\left[4a + (3/2)\,a^2\right] \tag{3}$$

where S, m, k, and T are the saturated surface density, molecular mass, Boltzmann's constant, and temperature, respectively. Although the carrier gas that is used to carry the reactant vapors to the substrate surfaces does not participate in the ALD reactions, it could affect the surface diffusion of reactants and thereby play a significant role in the ALD film growth.[41]

3. Challenges in Particle Modification via ALD

In order to obtain conformal and uniform coating films on the particles via ALD, it is crucial that the entire surface of target particles should be exposed to the reactant gases during the deposition cycle. However, the cohesive interparticle forces hinder the exposures of interior particle surfaces to the reactant gases during the ALD surface reactions, resulting in nonuniform coatings. As the particle size scales down to the nanoscale, cohesive interparticle forces become significant and strong, causing NPs readily adhere and form agglomerates or aggregates. Herein, the aggregation refers to the sintering together of particles, while agglomeration refers to the adhesion of particles.[42] A systematic explanation of agglomerates have been proposed by Yao et al., using the concept of multistage agglomerates theory (MSA).[42,43] According to the MSA theory, there exist three stages of agglomeration of particles. The first stage is the 3D netlike structure formed by primary particles (size < 10 μm) due to the strong aggregation effect. Then the netlike structure coalesces into simple agglomerates of micro size (size < 100 μm) due to the interparicle forces. The third stage is the formation of large and complex agglomerates (size > 100 μm) due to the physical motion in a reactor, such as fluidizing reactor. The formation of agglomerates is highly associated with the interparticle forces. Therefore, understanding the interparticle forces is crucial for optimizing process parameters to ensure effective PALD process. Typically, in a system of particles, chemical bonding is a strong force between particles. Except that, attractive forces also exist between the particles. Normally, there are four major interparticle forces, namely,

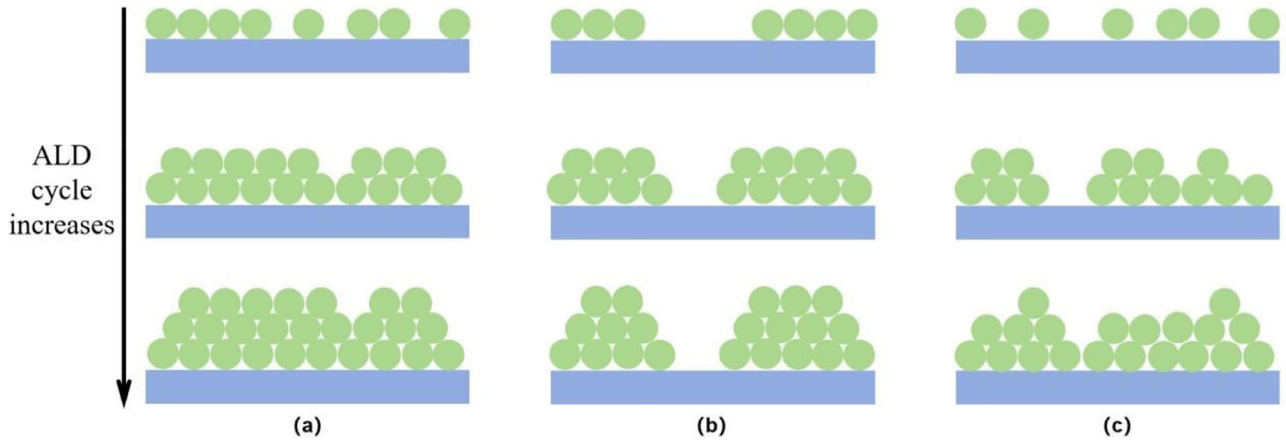

Figure 3. Schematic of the film growth mode in ALD. a) Two-dimensional growth mode, b) island growth mode, and c) random growth mode. Reproduced with permission.[35] Copyright 2005, AIP Publishing.

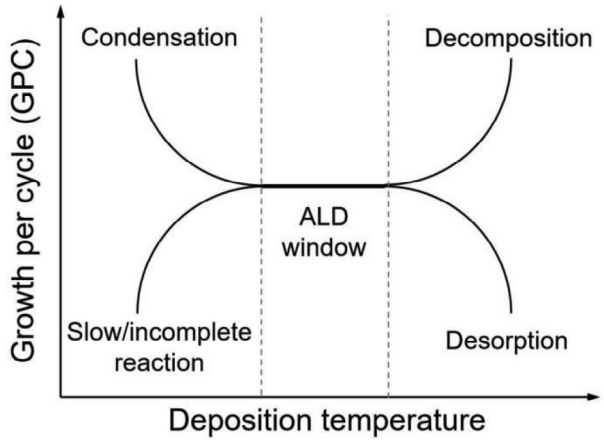

Figure 4. Schematic of the effect of deposition temperature on the growth per cycle (GPC). Reproduced with permission.[24] Copyright 2010, American Chemical Society.

van der Waals force, electrostatic force, liquid bridge formation, and sintering,[25] as listed in **Table 1**.

Van der Waals force is seen as a weak intermolecular force and plays a significant role in the attraction between the particles with the size less than 100 μm when two particles approach each other as closely as 1 nm.[25,44,45] Physically, the van der Waals force derives from the instantaneous nonuniform distribution of electronic charges on the particle surfaces. According to the simple model of rigid spheres, the van der Waals force in sphere–sphere interactions can be expressed as follows:

$$F_{vw} = \frac{A}{6d^2}\frac{R_1 R_2}{R_1 + R_2} \tag{4}$$

where A is the Hamaker constant (materials-related), which is an important parameter of the van der Waals force in describing the particle interactions including agglomeration and dispersion, R_1 and R_2 are the sphere radius of two particles, and d is the surface separation.[25,45] It implies that the van der Waals force increases as the surface separation distance decreases. In practice, the van der Waals force depends on the surface asperities and environmental dryness.

Electrostatic force can also arise among dry particles in a gaseous medium. In a dry environment, the opposite charges will

Table 1. Comparison of the main interparticle forces.

Force type	Origin	characteristics
van der Waals force	Instantaneous nonuniform distribution of electronic charges on particle surfaces	Significant at the very close separation distance (0.2–1 nm) Being affected by surface asperities and dry environment Particle diameter <100 um
Electrostatic force	Opposite charges on the particle surfaces induced by electron exchanging after contact, friction, collision, etc.	Force strength decreases rapidly as the separation distance increases, and increases with an increase in the charges carried on the particle surfaces Anisotropic particles exhibit a higher force than spherical ones due to the nonuniform charge distribution
Capillary force	Surface tension from the liquid–solid interface	Existing especially in the moisture environment Force strength increases with an increase in the surface tension
Sintering force	Material migration and strong bonding effects between the particles	Strong force to form dense particles which can hardly be separated Formation of "neck" in the region of contact

exist on the surfaces of the particles via electron exchanging after contact, friction, collision, etc. The electrostatic force F_{es} generated between the charged particles can be given by[25]

$$F_{es} = \frac{q_1 q_2}{4\pi\varepsilon d^2} \tag{5}$$

where q_1 and q_2 are the charges existed on the surface of the particles, ϵ is the dielectric constant of the medium between the particles, and d is the separation distance of the particles. The equation suggests that the force strength decreases rapidly with the separation distance, and increases with the charges carried on the particle surfaces. For anisotropic particles, the electrostatic force is larger than spherical ones due to the nonuniform charge distribution on surfaces. Also, the electrostatic force may exist between the reactor walls and particles, leading to the adhesion of particles on the reactor walls, which imparts the ALD process. Therefore, before ALD process, an anti-electrostatic treatment should be taken into account to avoid the accumulation of particles on the walls. To eliminate the effects of electrostatic forces, antistatic coatings are commonly used. Generally, a material with the surface resistivity of 10^5 Ω/□–10^{12} Ω/□ is defined as an anti static material.[46] Considering the operating conditions in PALD, some conductive materials such as metals (Ni, Ag, etc.) and metal oxide semiconductors (ZnO, SnO_2, etc.) are considered to be suitable for antistatic coatings for the reactors.[46–48] To obtain the antistatic coatings, some methods can be used, such as electroplating and spraying.[49,50] To deposit Ni-based conductive materials onto the surface of metallic reactors, electrodeposition could be a common method. To coat metal oxide semiconductors, the spraying method could be an option, especially for the reactor with complex shapes.[50] Plasma spraying is deemed to enhance anticorrosion performance of the reactors.[51] It is worthy to note that ALD is also an effective technique to coat pinhole-free and conformal films of metal oxide semiconductors as antistatic coatings, though the thickness of the coatings is usually at nanoscale.[52] Except the antistatic coatings and corresponding deposition methods, some other techniques benefit the mitigation of the static electricity. To electrically ground the reactors is an easy and reliable way which can dissipate the electrostatic charges. Although increasing the gas humidity in the reactors can increases the conductivity of the gas to reduce the static charges, it could induce the agglomeration of particles due to the liquid bridge formation which will be discussed later.

Due to the presence of water molecules between particles, there exists a solid-liquid interaction, resulting in the formation of liquid bridge as illustrated in **Figure 5**. The multiple particle bridging can lead to large agglomerates. Thus, the bridge formation affects the handling process of particles. The static force F_{ls} induced by the liquid bridge can be expressed as a sum of the surface tension and pressure drop[25]

$$F_{ls} = 2\pi r_2 \gamma + \pi r_2^2 \Delta P \tag{6}$$

$$\Delta P = \gamma \left[\frac{1}{r_1} - \frac{1}{r_2}\right] \tag{7}$$

where γ and ΔP represent the surface energy and pressure drop, respectively. r_1 and r_2 denote the principal radii of curvature of the liquid bridge surface. As the particles are close proximity to each other, the static force of the liquid bridge formation reaches the maximum value $F_{ls,\,max}$, given by

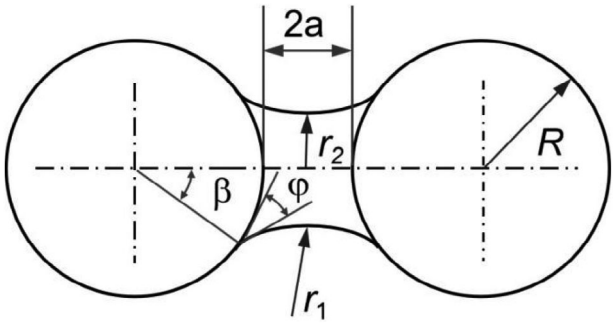

Figure 5. Schematic of the liquid bridge formation between two spherical particles. Reproduced with permission.[25] Copyright 2000, Elsevier.

$$F_{ls,max} = 2\pi R\gamma \tag{8}$$

where R represents the liquid bridge neck radius. The high humidity can have a severe effect on the liquid bridging. Hence, a drying step is required before the PALD coating. Moreover, in some dry processes, especially in the ALD process where water is used as reactants or the byproduct of the reaction, the possible liquid bridging formation becomes important, resulting in the formation of compact aggregates. Once the liquid bridging forms, the gas-solid interactions between reactants and particle surfaces will be reduced. Thus, proper reaction temperatures are required in the related ALD process to remove the water.

In ALD, high temperatures are usually used for drying particles and the coating process. At the elevated temperatures, the liquid bridging will be lost as the water is removed. However, the high temperature can give rise to the high rate of sintering among the particles. To some extent, sintering is as similar to the liquid bridging, except that the solid particles replace the water molecules in the "neck" region. The formation of "neck" in the sintering between particles is because that the material migrates to the region of contact. The particles with "neck" is often termed as permanent agglomerates or aggregates, meaning strong and dense particle collectives, which are hardly separated.[25,53] To describe the time-dependent sintering phenomenon, the neck radius x at a time τ can be expressed by the surface energy γ, particle radius r, and viscosity coefficient μ, according to the Frenkel equation for viscous sintering[53]

$$\left(\frac{x}{r}\right)^2 = \frac{3\gamma}{2r\mu}\tau \tag{9}$$

In the viscous sintering, migration is driven by the surface energy minimization and opposed by the viscosity. The viscosity is an Arrhenius function of the temperature[25]

$$\mu = \mu_0 exp\,(E/RT) \tag{10}$$

where E is the activation energy, T is the temperature, and R represents the molar gas constant. It indicates that the viscosity decreases with the temperature for the media in a liquid state, while the migration benefits from the temperature which facilitates the sintering. To this end, the viscous sintering occurs much faster

at higher temperatures. During the ALD process, the formation of sintering also reduces the degree of particle–reactant interactions, thereby leading to the non-uniform coating as the same as the liquid bridging does. Thus, careful reactor designs should be developed such that they can address the problems associated with interparticle forces as well as the process conditions.

To address the issue of agglomeration or aggregation induced by the cohesive interparticle forces, various strategies such as mechanical vibration, fluidization, and external field assistance have been developed.[2,54–57] For the vibration method, the vibration forces are exerted on the particles to cause them to be separated. Although the method suits for the particles with a wide size distribution, an appropriate thickness of the particle bed and layer phenomenon should be taken into account for the well separation. Fluidization is a method to flow the particles through continuously introduction of a upward gas to achieve the separation. However, some cohesive particles are difficult to reach a homogeneous fluidization state, which calls for external fields to improve the fluidization quality. In this respect, acoustic fields, electric fields and magnetic fields are applied to assist the fluidization.[57–59] These assistance fields also have their limitations. The use of acoustic fields may generate significant noise levels and potentially induce concerns about the joint tightness. The assistance of electric fields may bring safety problems associated with the use of high voltage and particle stability issues during charging/discharging process. Magnetic fields are limited to the particles that can be magnetized. Based on the advantages and disadvantages of these strategies, the combination of the one or two methods is deemed as a feasible option to separate the particles in the practical use.

Although the agglomeration or aggregation is one of the significant challenges in the surface modification of particles via ALD, there are also some other aspects that need to be considered, including the dependency of the film growth on irregular surfaced particles, and the low material utilization efficiency of reactants due to the prolonged dosage of reactants for a conformal coating. Regarding the ALD coating on irregular surfaced particles, granular films were mostly grown on the surfaces of particles, especially in the initial ALD cycles.[24] The properties of reactants such as the size of ligands and reactant vapor pressures also significantly affect the coating profiles.[60,61] In some cases, longer deposition time and lower reactant efficiency would occur, as using conventional ALD reactors for the particle coating.[62] In the system of particles at the reduced pressure, the pores between the particles are usually as small as sub-micrometer size, and the diffusion of reactant molecules enters the molecular flow regime.[63] Based on the mathematical deduction, Longrie et al. showed that the mass transfer purely by diffusion in the fixed particle bed can lead to as long as many hours to saturate the surface reaction sites for a complete coating.[26] Thus, mechanical agitation is required to enhance mass transfer, thereby reducing exposure time and improving reactant utilization efficiency. For instance, the fluidizing scheme for a large quantity of particles is demonstrated as an effective method to improve reactant utilization efficiency with losses of reactants limited to a few percent, verified by the experiments and simulations.[64,65] Although several approaches for agitation or fluidization of particles have been developed to enhance gas-solid interactions, reduce exposure times and improve reactant efficiency, designs of ALD reactors under atmospheric pressure is still challenging in PALD. On the other hand, robust design of ALD reactors for processing high-throughput particles is very promising for industrial sectors which often need to process tons of particles. Thus, scale-up solutions for PALD at atmospheric pressure or near atmospheric pressure have attracted much attention from the engineering sectors.

4. Reactor Designs for PALD

To address the problems associated with PALD, reactors used to hold the particle substrates and separation schemes of particles are crucial to a ALD system. Over the past decades, the interest in NP modification has pushed researchers to develop viable, easy-to-operate and even economically scalable PALD reactors. Successful modification of NPs have been achieved by using the designed reactors, although the reactors have their own advantages and limitations. Thus, in this section, the designs of reactors used in PALD will be discussed from the modeling approaches and lab-scale experiments to scale-up solutions.

4.1. Fixed-Bed Reactors

In 2000, George team attempted ALD coating on particles with a thermal ALD reactor.[66,67] A small quantity of particles was spread over the base of a fixed crucible (**Figure 6a**) while the reactant gases were injected from the upper to the bottom of the crucible. Due to the small quantity of particles, the reactant gases could diffuse through the interstitial of particles and thereby enable gas–solid interactions for the ALD surface reaction on the individual particles. As the amount of particles increased, it was found that only the top layer of particles could be successfully coated, leaving the bottom layer of particles uncoated, as shown in Figure 6b. For a complete coating of the entire particles, an extremely long time was needed because that it was difficult for reactant gases to diffuse deeply inside the particle bed, as the studies reported by Longrie et al.[26] To obtain the completion of coating for the bottom layer of the particle bed, George et al. proposed to place a photo-etched tungsten grid on the bottom of the crucible to support the particle substrates and let the reactant gases flow across the grid to the pump lines to ensure the exposures of particle surfaces at the bottom (inset of Figure 6c).[66] Since that the reactant gases could flow from the upper layer to the bottom layer of the particle bed, BN particles, including the particles on the bottom layer of the crucible, were successfully coated with ultrathin and conformal Al_2O_3 and SiO_2 films.[67] To some extent, the design of supporting the particle substrates with grids addressed the ALD surface reactions of the particles at the bottom layer of the crucible. However, this method had some drawbacks. Due to the fast flow rate, reactants usually tended to directly flow through the channels in the particle bed and be pumped out before the completion of ALD surface reactions, leaving some reactants unreacted. On the other hand, the amount of particles in the crucible was still small for the ALD coating process, limiting the application of ALD to process a large quantity of particles.

4.2. Fluidized Bed Reactors

To facilitate the delivery or diffusion of reactant gases to the particle surfaces, Wank et al. combined fluidization and ALD

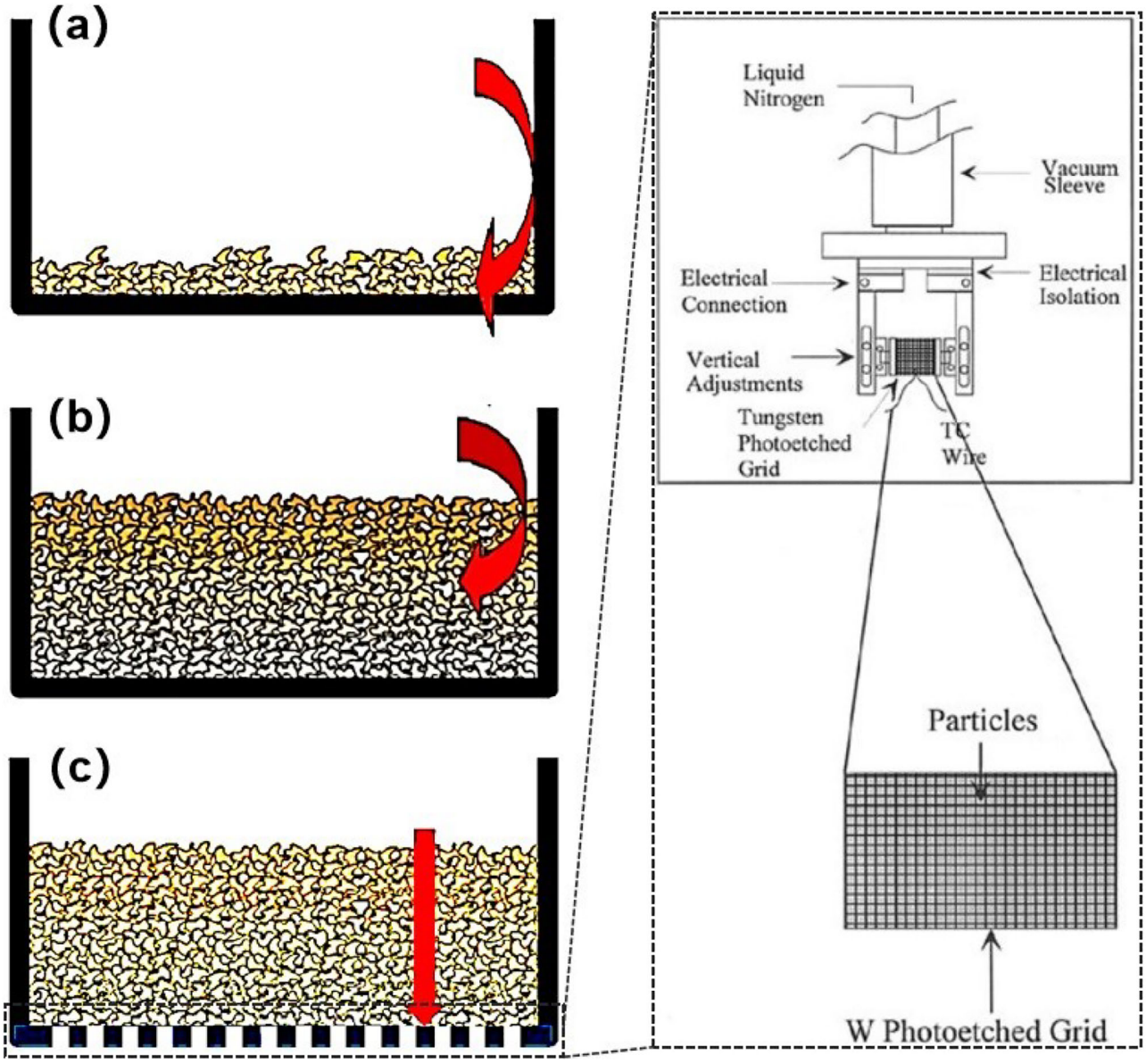

Figure 6. Schematic representation of fixed-bed reactors in ALD with particles inside the crucible. a) Individual particles are coated via ALD under conditions where a small quantity of particles is present in the crucible. b) Only the top layer of particles is coated via ALD for a larger quantity of particles. (Reproduced with permission.[26] Copyright 2014, American Vacuum Society. c) Particles at the bottom of the crucible can be coated using ALD if a tungsten photo-etched grid is used as a filter at the base. Reproduced with permission.[67] Copyright 2000, Elsevier.

technology together to coat films on particle surfaces. In 2004, they introduced a continuous upward gas into the FBR to disperse and suspend the particles, thereby successfully performing Al_2O_3 ALD surface reactions on micro-sized Ni and BN particles.[68,69] The continuous fluidization gas leads to intense interactions between reactants and particle surfaces, resulting in ALD surface reactions more efficient. In 2005, Weimer's group used FBR-ALD to successfully deposit conformal Al_2O_3 coating on silica (≈40 nm) and zirconia (≈26 nm) nanoparticles.[70,71] Their fantastic works were the first to show the world that the primary NPs can be coated by PALD technique and the fluidization scheme was important for this. Since then, the FBR-ALD opens up a feasible scheme of modifying NP surfaces in a gaseous medium.

4.2.1. Fluidization Basics

To fluidize particles, a continuous gas with a velocity of U is fed upward into the reactor, resulting in a pressure drop ΔP across the particle bed. The pressure drop will increase linearly with the gas velocity (**Figure** 7a, line OA). At a particular gas velocity, denoted as the minimum fluidization velocity U_{mf} (Figure 7a, point A), the particles will be floated and the pressure drop

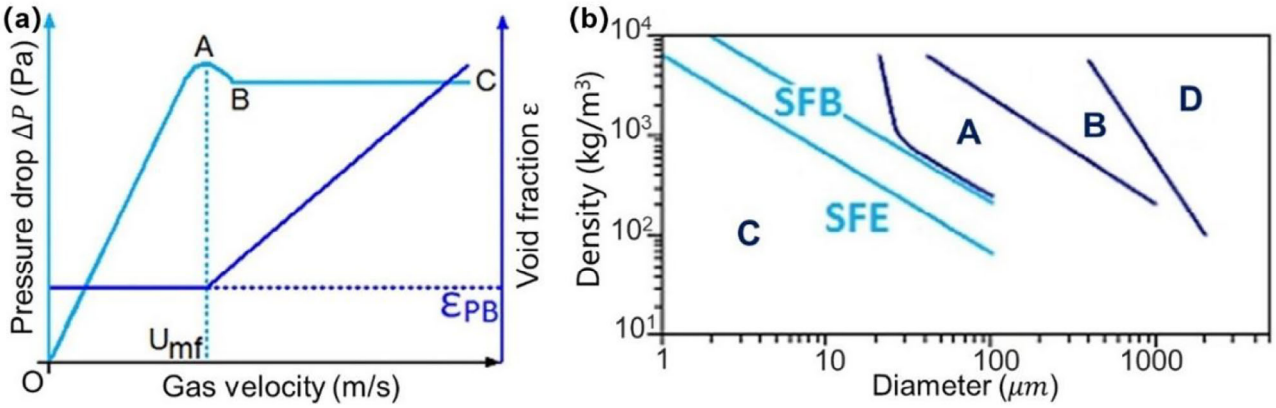

Figure 7. a) Pressure drop and voidage versus gas velocity. b) Extended Geldart diagram for powder classification with SFB (solidlike-to-fluidlike-to-bubbling) and SFE (solidlike-to-fluidlike-to-elutriation). Reproduced with permission.[26] Copyright 2014, American Vacuum Society.

becomes maximum. As the gas velocity increases slightly, the pressure drop will decrease a little. When the gas velocity increases further, the pressure drop will remain constant, reaching a fluidization regime (Figure 7a, line BC). At the fluidization regime, the voidage of particles increases with the gas velocity while the voidage merely changes before the fluidization. In the fluidized bed, the gravitational force is balanced by the drag force and buoyancy force induced by the fluidizing gas. The gas pressure drop ΔP across the bed area can be expressed as follows:[72]

$$-\Delta P = \frac{\text{weight of the particles} - \text{uptrust on the particles}}{\text{area of the bed}} \tag{11}$$

$$-\Delta P = H\left(1-\varepsilon_{mf}\right)\left(\rho_p - \rho_g\right) \tag{12}$$

where ϵ_{mf} is the voidage of the particle bed, ρ_p is the bulk density of the particles, and ρ_g is the density of the fluidizing gas. Using the Ergun equation[73] and laminar condition for a packed bed that the Reynolds number is less than 10,[72] the pressure drop across the height of particle bed is given by

$$\frac{-\Delta P}{H} = \frac{150 U_{mf}\mu}{\left(\phi d_p\right)^2}\frac{\left(1-\varepsilon_{mf}\right)^2}{\varepsilon_{mf}^3} \tag{13}$$

Thus, the minimum fluidization velocity based on individual particles can be expressed as

$$U_{mf} = \frac{\Delta P}{H}\frac{\left(\phi d_p\right)^2}{150\mu}\frac{\varepsilon_{mf}^3}{\left(1-\varepsilon_{mf}\right)^2} \tag{14}$$

Considering the equation of the pressure drop, the minimum fluidization velocity can be obtained as

$$U_{mf} = \frac{\left(\phi d_p\right)^2}{150\mu}\left[g\left(\rho_p - \rho_g\right)\right]\frac{\varepsilon_{mf}^3}{1-\varepsilon_{mf}} \tag{15}$$

where ϕ is the sphericity, d_p is the particle (or agglomerate) diameter, μ represents the dynamic viscosity, ϵ_{mf} is the porosity at the minimum fluidization, and g is the gravitational acceleration. It indicates that U_{mf} increases with the particle size d_p and particle density ρ_p, and is affected by the properties of the fluidizing gas. The minimum fluidization velocity is a crucial parameter of the fluidization behavior to enable gas–particle interactions.

Generally, there are two fluidization regimes in the fluidizing particles: homogeneous fluidization (i.e., no-bubbling) and bubbling fluidization. In the homogeneous fluidized bed, the particle–particle distance will increase with the gas velocity while the pressure drop across the bed remains constant. The bubbling fluidized bed is typically composed of two distinct phases: the bubbling phase which contains gas bubbles and emulsion phase which consists of fluidized particles surrounding the bubbles.[74,75] In the bubbling fluidization, the gas with the velocity exceeding U_{mf} will pass through the particle bed as bubbles. The minimum bubbling velocity U_{mb} represents the gas velocity which make bubbles start to appear in the fluidized bed.

To classify and predict the fluidization behaviors of particles, Geldart divided particles into four categories, denoted C, A, B, and D, as cohesive, aeratable, bubbling, and spoutable, respectively,[2,76] as shown in Figure 7b. According to the classification, the very fine and cohesive particles belong to the Geldart type C, which cannot be homogeneously fluidized due to the strong interparticle forces, resulting in formation of plugging and/or channeling in the particle bed. Since the cohesive particles or NPs tend to form agglomerates, the structure of agglomerates affects the fluidization behaviors more significantly compared to individual NPs. In this respect, the fluidizing entities are agglomerates rather than individual particles. There are two major phenomena occurring during the agglomerate fluidization, namely, agglomerate particulate fluidization (APF) and agglomerate bubbling fluidization (ABF). APF refers to the high expansion bed and no-bubbling fluidization for the light and porous agglomerates, behaving like the particles of Geldart type A. On the other hand, ABF exhibits fluidization behavior like Geldart type B particles and only macroscopic bubbles are formed, leading to an inhomogeneous expansion bed. Yao and Zhu et al. summarized the comparison of fluidization behaviors between APF and ABF.[42,77]

For the particles in the classical Geldart type C, there are some important findings which could help to improve the understanding of the fluidization behaviors of these particles.

As illustrated in Figure 7b, there exist two subcategories for cohesive particles depending on the particle size and relative density, namely, solidlike-to-fluidlike-to-elutriation (SFE) and solidlike-to-fluidlike-to-bubbling (SFB).[76,78,79] The SFE behavior means that the particle bed consisting of light and small particles will expand homogeneously without the formation of the bubbling before the elutriation of particles, while SFB behavior means that the particle bed comprising heavier and larger particles will generate bubbles when the gas velocity increases above the fluidlike state.

In the fluidized bed, it should be noted that fine particles or NPs are not fluidized individually, but as particle agglomerates. As discussed in the MSA theory, the formation of particle agglomerates is dynamic during the fluidization, showing the continuous disintegration and reformation of complex agglomerates, because of the shear forces exerted by the fluidizing gas and the collisions between circulating agglomerates.[42] After the investigation of fluidization behaviors of various nanopowders at atmospheric and reduced pressure, Hakim et al. used dynamic aggregation to describe the phenomenon that NPs could shed from one agglomerate to another.[80] Later, Hakim et al. further pointed out that the dynamic aggregation of NP agglomerates in the fluidized bed highly facilitated the ALD coating process and made the PALD process viable.[70] It is worthy to note that the surfaces of NPs inside the agglomerates can be exposed to the reactants in a short time due to the continuous recirculation and frequent collisions between the particle agglomerates.[71] To break particle agglomerates, prolonged exposure time facilitates the reactions of reactant gases with surface active sites, while extended purging time is conducive to the removal of unreacted gases within the agglomerates. Regarding the transport of reactant gases inside porous agglomerates, similar to the case inside a pipeline, there is an important parameter for the transportation behavior of molecules, denoted as Knudsen number K_n, which is defined as[81]

$$K_n = \frac{\lambda}{L} \tag{16}$$

where L is the average pore diameter and λ is the mean free path (MFP) of the reactant molecule which can be expressed as[82]

$$\lambda = \frac{k_B T}{\sqrt{2}\pi\sigma^2 P} \tag{17}$$

where k_B is the Boltzmann constant, T is the temperature, σ represents the molecule collision diameter, and P is the pressure. It indicates that the MFP is closely related to temperature, pressure and molecular diameter. Considering the complex shapes of NPs, Grillo et al. developed a model to describe the diffusion behavior in NP agglomerates which can be treated as a porous media.[65] According to the MSA theory, there exist three stages of NPs, namely, aggregates, simple agglomerates, and complex agglomerates.[42] Based on the three-level hierarchical structure, they proposed two levels of the precursor diffusion at the NP agglomerates, namely, the complex-agglomerate level characterized by the porosity of 0.77, and the simple-agglomerate level characterized by the porosity of 0.95. It was concluded that, at the atmospheric-pressure, the diffusion process was in Fickian regime for the complex agglomerates and in transition regime (both Knudsen and Fickian diffusion) for the simple agglomerates. Under the low pressure of 1 mbar, the diffusion process entered transition regime at the complex-agglomerate level while the Knudsen regime was fully developed at the simple-agglomerate level.[65] Furthermore, different diffusion regimes lead to different time scales. Grillo et al. put forward six time scales, including gas residence time in the emulsion phase and bubble phase, the diffusion time at simple-agglomerate level and complex-agglomerate level, and the like.[65] In their study on the bubbling fluidized bed for a batch of 22 g TiO_2 NPs, they found that, at the atmospheric pressure, the time scale of TMA half reaction was shorter than that of the diffusion at the complex-agglomerate level. However, under the low pressure of 1 mbar, the reaction time scale became equivalent to the diffusion at the both complex and simple agglomerates, and almost the reaction and transport processes became faster.[65] Similarly, Duan et al. pointed out that, in the fluidized bed, the diffusion time of reactant gases inside the particle agglomerates can be negligible compared to the much longer reactor scale diffusion time under the vacuum condition.[83]

Now as the basics of the fluidization has been discussed, the size of particle agglomerates is crucial to predict the fluidization quality in the fluidized bed. In order to estimate the mean size of particle agglomerates during the fluidization, some methods have been developed based on the force balance model,[84] energy balance model,[85] and Richardson-Zaki (R-Z) equation.[77,86,87] Apart from the agglomerate size, the voidage and agglomerate density can be estimated according to the modified R-Z equation.[86] To enhance the fluidization quality, various external force have been developed to assist the fluidization, such as mechanical agitation,[64] electric field,[58] magnetic field,[57,88] vibration,[69,89,90] acoustic wave,[55] etc. And these assistance forces can be also used in the FBRs to facilitate the ALD process.

4.2.2. Designs of Fluidized Bed Reactors

In comparison to the conventional reactors, the major advantage of FBR lies in the efficient gas-solid interactions, resulting in high rates of heat and mass transfer. The first attempt to use FBR for the ALD process was developed by Wank et al. in 2004.[68] In their work, they successfully obtained conformal Al_2O_3 films on nickel particles (150 µm) by combining fluidization and ALD techniques. According to the classical Geldart diagram, the selected nickel particles with the diameter of 150 µm belong to the Geldart type A, exhibiting easy fluidization. Later, they improved the design of FBR to adapt to coating cohesive boron nitride (BN) particles, belonging to the Geldart type C, with the wide size range from 7 to 60 µm.[69] In their design, the added vibration motors were attached to the FBR for prompting the fluidization behavior of cohesive BN particles, and the inert gas was used as both the fluidizing gas and purging gas through the dosing line. Due to the dynamic aggregation of BN particles during the fluidization, an ultrathin and conformal Al_2O_3 film had been deposited on individual BN particles through ALD.[69]

To optimize the ALD process, King et al. designed a fluidized bed ALD system using a mass spectroscopy for real-time mon-

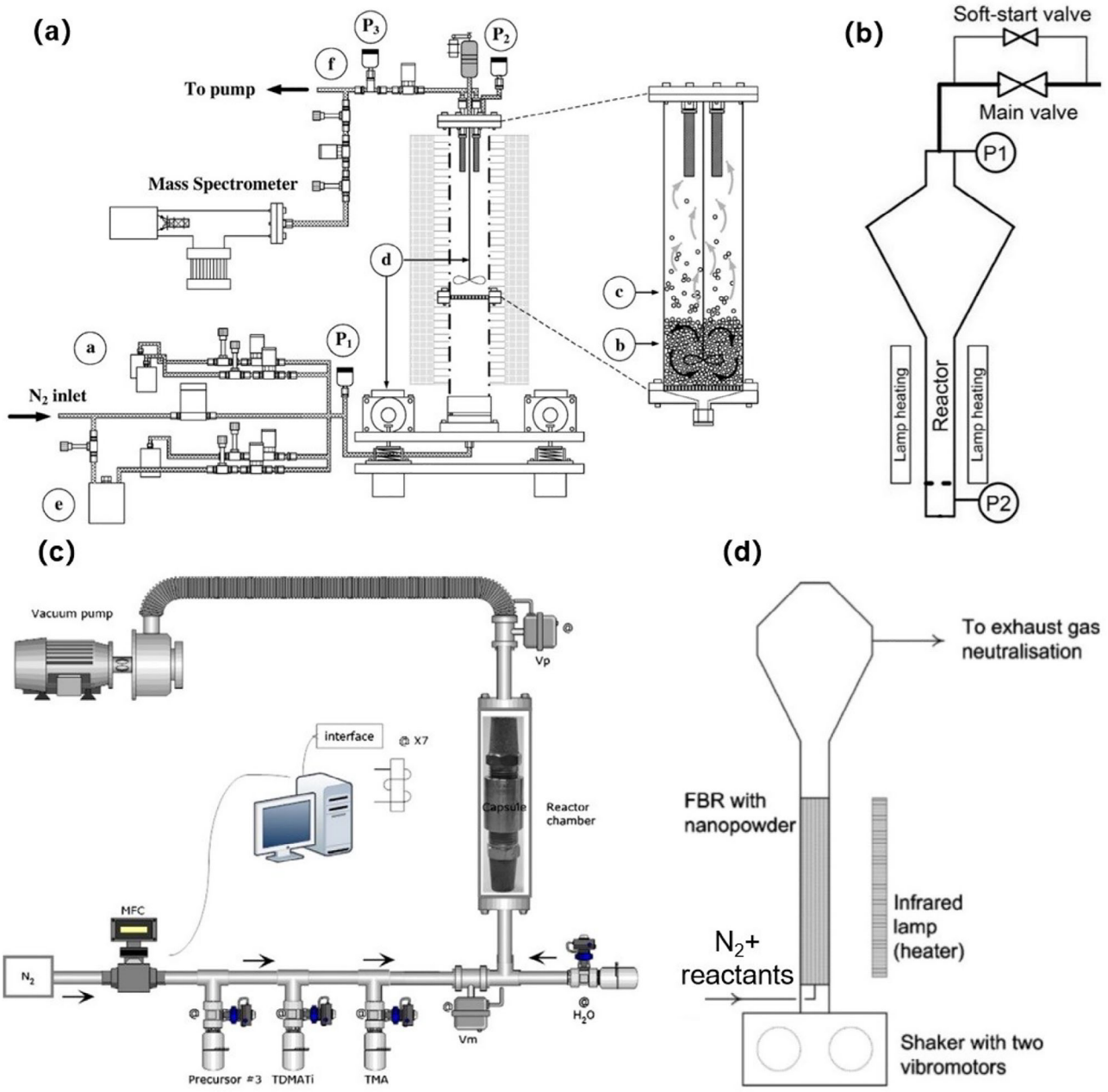

Figure 8. Schematic representation of the designs of fluidized bed reactors for ALD process. a) Experimental set-up for a fluidized bed reactor with vibration and mechanical stirring. Reproduced with permission.[64] Copyright 2007, Elsevier. b) The fluidized bed reactor with a specific taper design. The upper part of the reactor tube is expanded at an angle of 25° with respect to the axis of the tube, resulting in dramatic decrease of the gas velocity and thereby preventing particle and agglomerate entrainment. Reproduced with permission.[93] Copyright 2014, AIP Publishing. c) Experimental setup of a pulsed-bed ALD reactor. Reproduced with permission.[96] Copyright 2014, Elsevier. d) Schematic drawing of a fluidized bed reactor that can be operated at the atmosphere pressure. Reproduced with permission.[97] Copyright 2009, Wiley-VCH.

itoring of film growth characteristics.[64] In **Figure** 8a, a mass spectrometer was attached to the outlet of the FBR, which was equipped with magnetically-coupled mechanical stirring and vibration motors for promotion of fluidizing NPs and micro-sized particles. The authors pointed out that the FBR can be employed to deposit many types of films on the various particle substrates including metals, ceramics and polymers. Moreover, with the in situ monitoring of ALD reactions, near 100% utilization of the specific precursor can be attained under optimized process conditions.[64] Similarly, Duan et al. found that the utilization efficiency of TMA and H_2O can reach 99% under the optimal fluidization process.[83] Grillo et al. presented a multiscale dynamic model to understand and optimize the precursor utilization during PALD and the results showed that hardly any loss of precursors could be obtained at the proper operating conditions.[65] However, in the semiconductor industry, the use efficiency of

precursors is usually reduced to ≈50%[91] due to the bypass of costly precursor gases around the planar substrate surface, making ALD a more expensive option.[92] Actually, FBRs are preferred for high utilization efficiency of precursors since all feed gas flows through the particle bed. Therefore, FBR-ALD is deemed as a low-cost process for particle modification, as discussed in a recent paper of Dr. Weimer.[92] In the typical FBR, a porous distributor plate beneath the reactor is usually needed to prevent the particles from falling into the pipelines, and the filters placed in the top of the reactor are required as well to avoid the entrainment of particles due to the particle elutriation. In a specific design of FBR designed by Didden et al., the filters in the top of the reactor were eliminated.[93] To prevent the particles from getting entrained by the gas flow, the FBR was designed to have an expanded upper tube with the expanded angle of 25° with respect to the axis of the lower tube, as shown in Figure 8b. Because of the drastic decrease of the gas flow velocity in the expanded upper tube, most of particles and particle agglomerates could be prevented from being carried away to the exhaust. In addition, a pneumatic piston vibrator was installed on the bottom of the reactor to improve the fluidization behaviors. With the designed ALD apparatus, they successfully achieved TiO_2-coated SiO_2 core–shell NPs with homogeneous shells.[93]

In FBR-ALD, the purge time and dose of reactant gases should be harmonized with the appropriate upward gas velocity to sustain the fluidized state of particles. However, the initial conditions of the particle bed, like bed mass, particle size, and agglomerate kinetics, vary from one particle bed to another, resulting in different processing parameters for specific particles to be coated.[64] To address these problems, pulsed-bed fluidization was established from experiment and modeling.[94,95] With combining the pulsed-bed fluidization and ALD, Tiznado et al. designed and developed a pulsed-bed ALD system (Figure 8c).[96] The pulsed-bed reactor was designed as a reaction chamber with a closely fitted capsule, which was assembled by two opposite filters. Since that the capsule nearly occupied the entire inner volume of the reaction chamber, the reactant gases were forced to flow through the capsule. In the set-up, two valves, namely, V_p and V_m, were installed before and after the reaction chamber. Through controlling the open and close of the two valves, the violent turbulent flow was established in the reaction chamber and thereby caused an expansion of the particle bed in the capsule. Plus the dosing and purging steps, the ALD reaction was completed in the reaction chamber. Using the pulsed-bed ALD reactor, the authors achieved conformal Al_2O_3 films on the particles with different morphological characteristics, such as carbon nanotubes, flower-like ZnO micro-arrays, and $YCrO_3$ particles, indicating that the pulsed-bed was appropriate for a small quantity of particles and served as a very convenient alternative for research purposes.[96]

For the conventional fluidized ALD, the operation pressure requires at the reduced pressure due to the reactant vapor pressure usually on the order of 1–10 Torr.[64,69] Consequently, the expensive vacuum equipment is needed to maintain the reduced pressure in the ALD system. However, working under atmospheric pressure provides a cheaper and less complicated solution for the fluidized bed ALD system. In 2009, Beetstra et al. developed a FBR-ALD system which could work at atmospheric pressure.[97] In their design (Figure 8d), the effluent gases from the reactor were led through a double set of gas washers which was used to deal with the excessive reactants and reaction byproducts. And the pressure at the outlet of the ALD system was atmospheric. To improve the fluidization quality, the vibromotors were installed on the bottom of the reactor to provide vibration assistance. Using the designed ALD apparatus, a batch of 120 g $LiMnO_4$ particles with the size of 200–500 nm had been successfully coated with conformal Al_2O_3 films. Later, Goulas and Ommen employed a similar ALD system to decorate TiO_2 NPs (21 nm) with nanostructured Pt clusters,[98] indicating that the FBR-ALD working at atmospheric pressure was an attractive technique from the perspective of the scale-up potential. In order to obtain good fluidization of particle agglomerates, vibration motors were also employed in the atmospheric-pressure FBR-ALD system. Recently, Soria-Hoyo et al. devised a non-assisted FBR-ALD that can operate at atmospheric pressure to modify the surfaces of nanosilica particles with CaO films.[99] The absence of external assistance methods, such as vibration, was because that nanosilica particles could be uniformly fluidized at the optimum range of the fluidizing gas velocity, ensuring the effective gas-solid interactions in the system.[99]

4.3. Rotating Bed Reactors

In the fluidization scheme, to float the individual particles, the upward force induced by the fluidizing gas needs to be equal to the gravitational force of the particle. To this end, the fluidizing gas needs to be continuously introduced into the reactor and thereby applies drag forces on the particles. Due to the fast flow rate in the FBR, the residence time of reactants may be too short to reach high efficiency for some reactants with low reactive sticking coefficients in the ALD surface reactions.[100] With sufficient exposure times, the reactants even with the low reactive sticking coefficient can react with the particle surfaces completely. Moreover, to avoid the agglomeration of particles caused by coating films, it is necessary to disperse the particles during the ALD process. To solve these issues, a rotary reactor enables both static reactant exposure and necessary agitation for the PALD process.

In 2006, McCormick and George et al. developed a rotary reactor for thermal ALD growth on particles.[101,102] As shown in **Figure 9a**, the rotary reactor mainly includes multiple-input dosing flange, cylindrical drum with porous stainless steel wall and magnetically coupled rotary manipulator. The cylindrical drum was used to support the particle substrates and could rotate with the magnetically coupled rotary manipulator. And the mean diameter of the pores was 10 μm in the porous walls of the cylindrical drum. As the reactant gas being dosed from the multiple-input dosing flange into the chamber, the gas could flow through the porous walls of the cylindrical drum to react with the particle surfaces. As illustrated in Figure 9b, the particle in a porous vessel experiences inward viscous drag force for gases entering the porous wall, outward centrifugal force for rotating motion and gravity. At a low-speed rotary reactor in which the centrifugal force is less than the gravity force, the particles in the reactor are lifted up first and then fall off from the wall. In this way, the particles are dispersed during the ALD process. On the other hand, within a reactant pulse period, the valve on the outlet is closed to provide sufficient residence time of reactants for the completion of ALD reactions on the particle surfaces. With the novel ro-

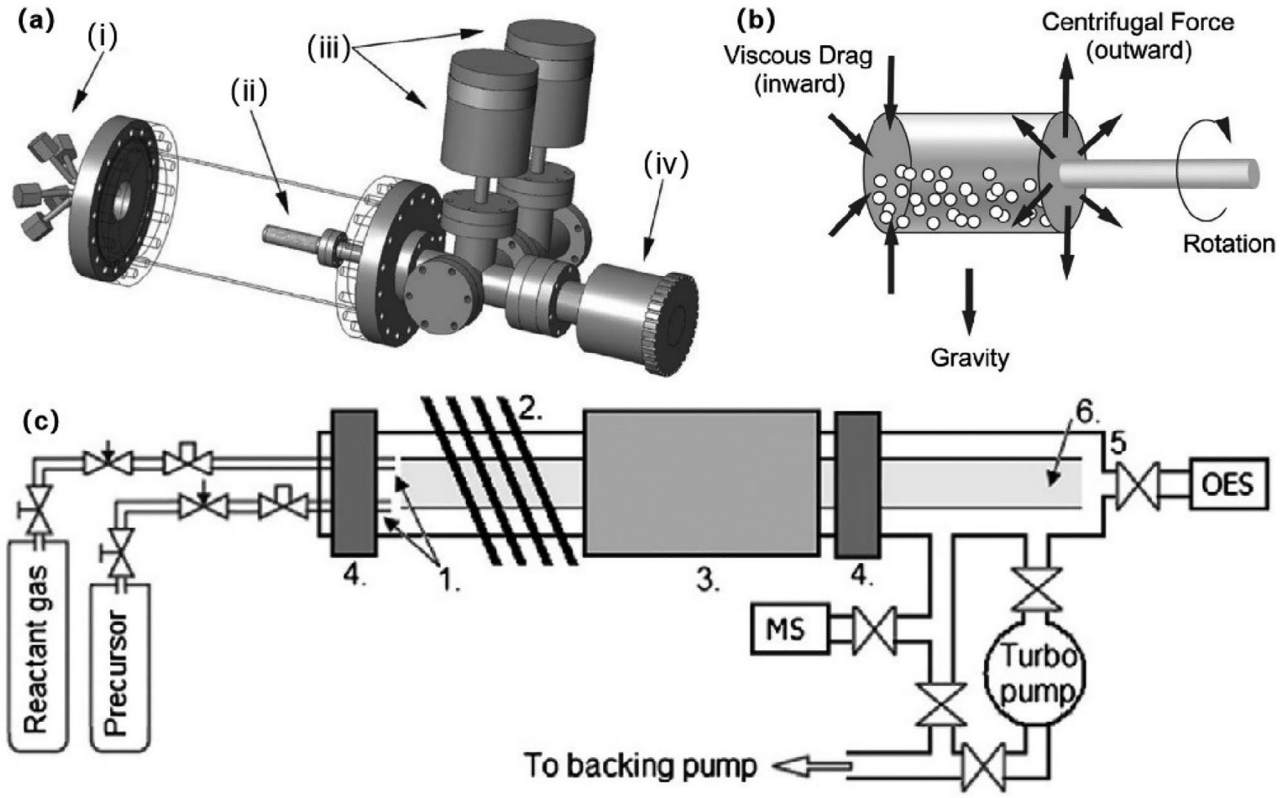

Figure 9. Designs of rotating bed reactors. a) Design of a rotary reactor with multiple-input dosing flange (i), rotated cylindrical drum with porous stainless-steel wall (ii), capacitance manometers (iii), and magnetically coupled rotary manipulator (iv). Reproduced with permission.[101] Copyright 2007, American Vacuum Society. b) Schematic representation of a rotating bed reactor under the rotation of the reactor in which the powder suffers the inward viscous drag force, outward centrifugal force, and gravity. Reproduced with permission.[101] Copyright 2007, American Vacuum Society. c) Schematic diagram of a radical-enhanced rotary reactor consisting of multiple-input flange (1), RF coil (2), tube furnace (3), mechanical rotation system (4), outer quartz tube chamber (5), and inner glass tube for supporting the particles. Reproduced with permission.[103] Copyright 2012, Elsevier.

tary reactor of ALD, they obtained conformal Al_2O_3 film on ZrO_2 particles.[101,102] Compared to the fluidization scheme, the rotary reactor scheme utilizes a static stream of reactant gases and agitates the particles by the rotating motion of the substrate bed. Hence, the efficiency of source reactants is supposed to be higher than the fluidization scheme.

A second type of rotary reactor for performing ALD was designed by Longrie et al. in 2012.[103] Compared to the rotary reactor developed by McCormick and George et al., they applied an open glass tube which was placed inside the quartz tube chamber to support the particle substrates, instead of the metal-made cylindrical reactor and chamber. This design rendered ALD using the inductively coupled RF plasma possible, which extended the use of thermal ALD process. Specifically, the designed rotary reactor consisted of multiple-input flange, RF generator, tube furnace, outer quartz chamber, inner glass tube, mechanical rotation system, and tube furnace (Figure 9c). The inner glass tube coupled to the outer quartz tube was open and used to support the particles to be coated. The mechanical rotation system provided the agitation of the particles. The RF generator which generated remote plasma was composed of RF coil, power supply and matching unit. The RF coil was placed around the outer quartz tube, and arranged between the gas inlet and the tube furnace, in order that the radicals generated by the RF coil could be delivered to the particle area. Due to the high vacuum condition (base pressure $<1 \times 10^{-5}$ mbar) ensured by the vacuum system composed of a backing pump and a turbo molecular pump, the purging steps with the inert gas in the ALD process were eliminated. Using the thermal and plasma-enhanced ALD system, the authors demonstrated the effectiveness of the ALD process to deposit Al_2O_3, TiO_2, and AlN films on various particles, such as ZnO NPs, micron sized stainless 316L particles, titanium granules and mm-scale spherical glass beads.[103] Due to the use of plasma-enhanced ALD, this rotating bed reactor can be used to coat particles at lower temperatures. On the other hand, because of the reduced conformality as compared to thermal ALD, plasma-enhanced ALD can be used as selectively coating on porous particle surfaces without coating the interior surface of the pores. Also, it can be applied in the catalysis field to modify the particle surfaces with reactive sites selectively, showing extensive potentials in the modification of particle surfaces.[103]

4.4. Rotating Fluidized Bed Reactors

In rotating bed reactors, the centrifugal force induced by the rotating motion is usually less than the gravity force of the particles, thus the particles can be lifted up and then fall off from

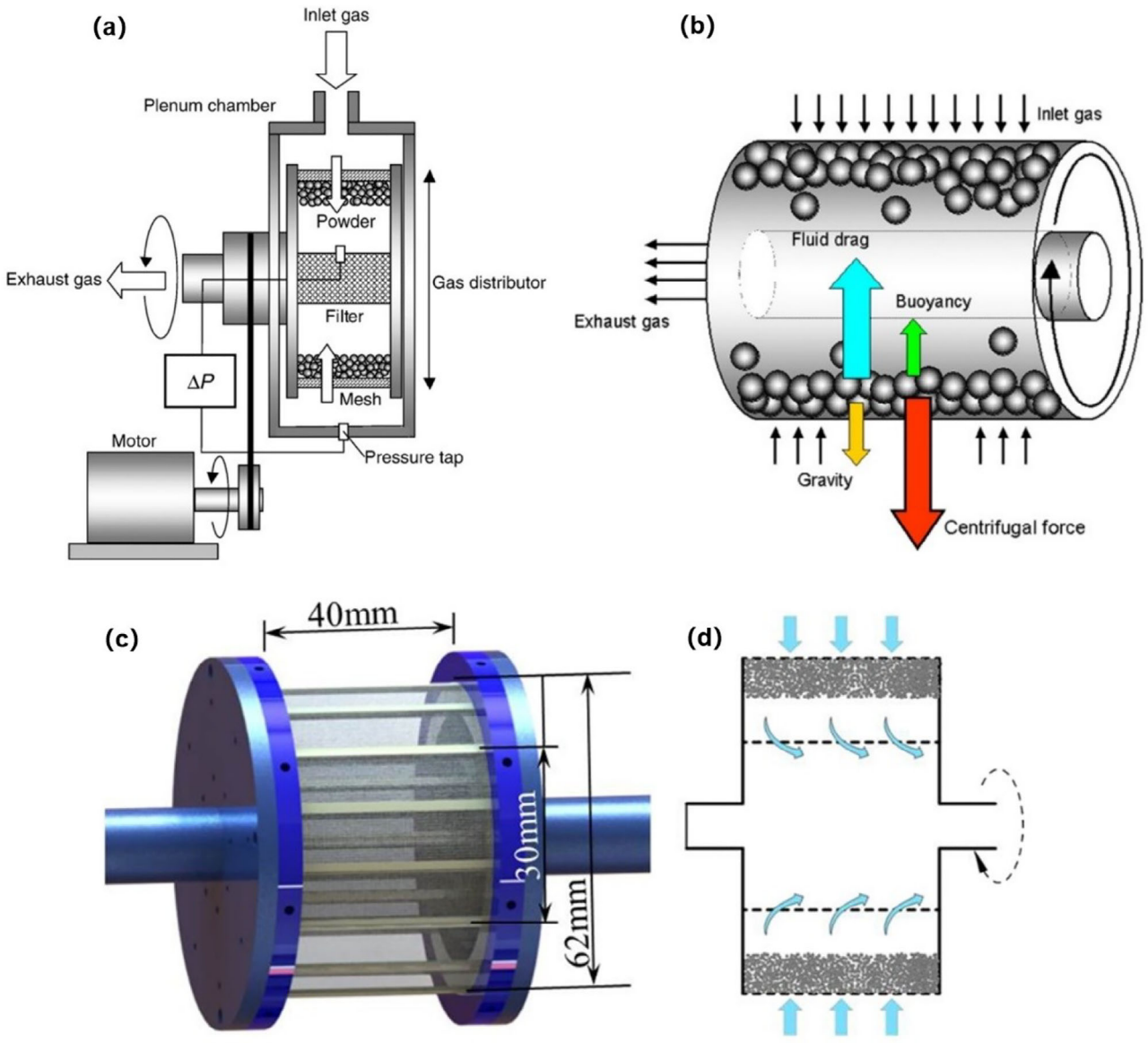

Figure 10. Designs of rotating fluidized bed reactors. a) Schematic diagram of a rotating fluidized bed reactor with a radial gas injection and an axial gas exhaust, and b) different forces acted on the particles. Reproduced with permission.[105] Copyright 2008, Elsevier. c) Design of a rotating fluidized bed reactor with double cartridges, and d) directions of gas injection and exhaust in the designed reactor. Reproduced with permission.[106] Copyright 2015, AIP Publishing.

the wall of rotating bed reactors. As the rotation speed increases appropriately and a pressure drop can be established under the gas flow, the particles inside the rotating bed can be fluidized. Based on this consideration, Watano et al. proposed a novel rotating fluidized bed system in 2003.[104] As illustrated in **Figure 10a**, the rotating fluidized bed consisted of a plenum chamber and a horizontal cylinder which was made of a porous cylindrical air distributor. The horizontal cylinder, which was used to support particles, could rotate around its axis of symmetry inside the plenum chamber. With the centrifugal force, the particles formed the annular bed near to the rotating vessel. The inlet gas was introduced from the nozzle on the plenum chamber, flowed inwards through the air distributor and was pumped out from the center of the rotating cylinder. The inlet gas acted on the particles and gave rise to the drag force and buoyancy. In the rotating fluidized bed (Figure 10b), the gravity is balanced by the centrifugal force and the forces induced by the air flow (drag force and buoyancy).[104,105] However, in the conventional fluidized bed, particles are lifted up by a vertical airflow, resulting that the drag force and buoyancy are balanced by the gravity force. Watano et al. pointed out that the rotating fluidized bed system could reduce the size of NP agglomerates and led to well dispersion of NPs.[105]

Based on the fundamentals of rotating fluidized bed, Chen et al. designed a fluidized bed coupled rotary reactor for ALD on NPs in 2015.[106] In Figure 10c, the rotating FBR was com-

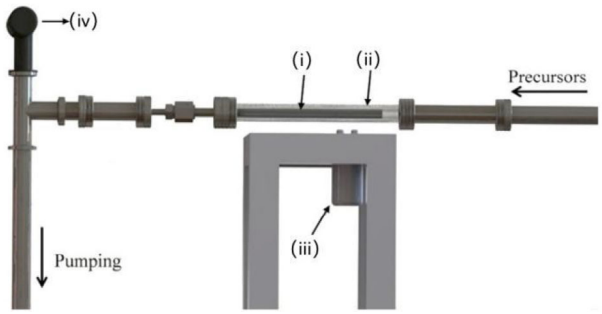

Figure 11. Schematic diagram of a vibration bed reactor, including (i) porous stainless-steel particle-loading cylinder, (ii) accommodation cylinder fitted by ConFlat flanges, (iii) pneumatic linear vibrator, and (iv) pressure gauge. Reproduced with permission.[89] Copyright 2014, American Vacuum Society.

posed of a cylindrical cartridge which used an outer and an inner mesh of 40 mm in length, while the diameters of the outer and inner mesh were 62 and 32 mm, respectively. The meshes were braided by a stainless steel with pores about 2–3 μm and thickness about 80 μm, and supported by the homocentric frames of which one end was attached to the shaft of the rotary manipulator. Thus, the particles were held between the double meshes and the outer mesh acted as an air distributor while the inner mesh as a filter. As displayed in Figure 10d, the fluidized gas flowed into the cartridge radially, and the drag force acted on the particle bed was opposite to the centrifugal force. With a proper rotating speed and an inlet gas speed, the particle bed exhibited stable fluidization when the centrifugal force was balanced by the gas drag force. With the experimental setup, the authors demonstrated successfully ALD Al_2O_3 coating on SiO_2 NPs and CeO_2 nanopolyhedras.[106]

4.5. Vibrating Bed Reactors

Besides the FBR and rotary bed reactor, Park et al. proposed another scheme for the ALD reactor by employing an external vibrator attached outside the reactor.[89] In the vibrating scheme, the intense vibration during the deposition cycles induced the effective separation of particles, which overcomes the interparticle forces in the particle agglomerates and thereby enables gas-solid interactions for the ALD reaction. As shown in **Figure 11**, a porous stainless steel cylinder used as loading substrate particles was placed inside a ConFlat flange-type accommodation cylindrical chamber, and a pneumatic linear vibrator was attached onto the outside cylinder to generate the vibration force. In order to absorb the chamber vibration, the chamber was connected to the reactant and pump lines via flexible bellows. Using the setup apparatus, they successfully conducted the ALD deposition of Al_2O_3 with the thickness of 10–15 nm on acetylene black particles with diameters of 200–250 nm and the vibration forces or frequencies were evaluated to optimize the process conditions. The higher vibration frequency or stronger vibration force facilitates the ALD reaction, as it promotes good separation during the deposition, thereby overcoming the interparticle forces and enabling effective delivery and diffusion of reactant gases into the particle bed. It is worthy to note that vibration is usually used as one assistant method for separation of particles in FBR-ALD system.[64,69]

4.6. s-ALD Reactors

The above-mentioned ALD reactors are deemed as t-ALD reactors, in which the reactants are sequentially dosed into the same reactor and followed by intermittent purging steps. In contrast to t-ALD reactors, s-ALD reactors allow simultaneous dosing of reactants into different locations. To achieve the s-ALD process, three main schemes can be adopted, which are physically separated half-reaction zones, movement of the substrate or gas injector head, and a barrier between the half-reaction zones.[30,107,108] Until now, several typical s-ALD apparatus have been developed for flexible substrates, such as roll-to-roll s-ALD, rotating central drum s-ALD, and close proximity s-ALD, where the inert gas was used as the curtain barrier between different reactant regions.[30,108]

In the laboratory experiment, the volume of particles to be dealt with ALD is usually small. Therefore, the laboratory-scale ALD reactors are sufficient to modify the particles. However, in industrial-scale mass production, the particles to be processed are usually hundreds or thousands of tons, necessitating scale-up production solutions for PALD. The continuous s-ALD reactor designs facilitate the mass production. In these reactors, the particles can be continuously added into these types of reactors, meanwhile the modified particles can be drawn from the reactors in time without shutting down the whole ALD apparatus.

Until now, several prototypes based on continuous s-ALD have been developed for processing high-throughput particles. One US patent filed a design of gravity-induced semi-continuous s-ALD reactor (**Figure 12**a,b).[109] The s-ALD reactor consisted of several particle reservoirs which were placed vertically, and therefore the particles could pass through from the upper reservoir to the lower one driven by the gravity. The ALD half-reactions were completed sequentially in different reservoirs with different reactants, while the purging steps were carried out between the half-reactions during the falling of particles. Since that the particles experienced half-reactions and purging steps successively, this type of reactor could be deemed as gravity-induced progressive ALD reactor which can be used in semi-continuous processing of the particles. The drawbacks of this kind of ALD reactors might be in that more ALD cycles require more reservoirs and greater height of the whole ALD reactor as well. Another s-ALD was proposed to apply inert gas (such as N_2, etc.) to transport the particles for continuous yield of coated particles, in which the reactants A and B were dosed into the conveying path of the particles alternately.[26] Based on this concept, in 2015, van Ommen et al. developed a 27 m long and 4 mm inner diameter tube as a pneumatic transport line reactor that could be operated at atmospheric pressure.[110] The reactor consisted of three major parts (preheating zone, reactant reaction zone and co-reactant reaction zone), with N_2 gas transporting the substrate particles through the system (Figure 12c). Via the designed s-ALD reactor, the researchers successfully deposited Pt nanoclusters with ≈1 nm diameter onto TiO_2 NPs. Due to the elimination of purging steps, the processing rate of TiO_2 NPs can reach about 60 $g \cdot h^{-1}$.[110] For making the particles move between dif-

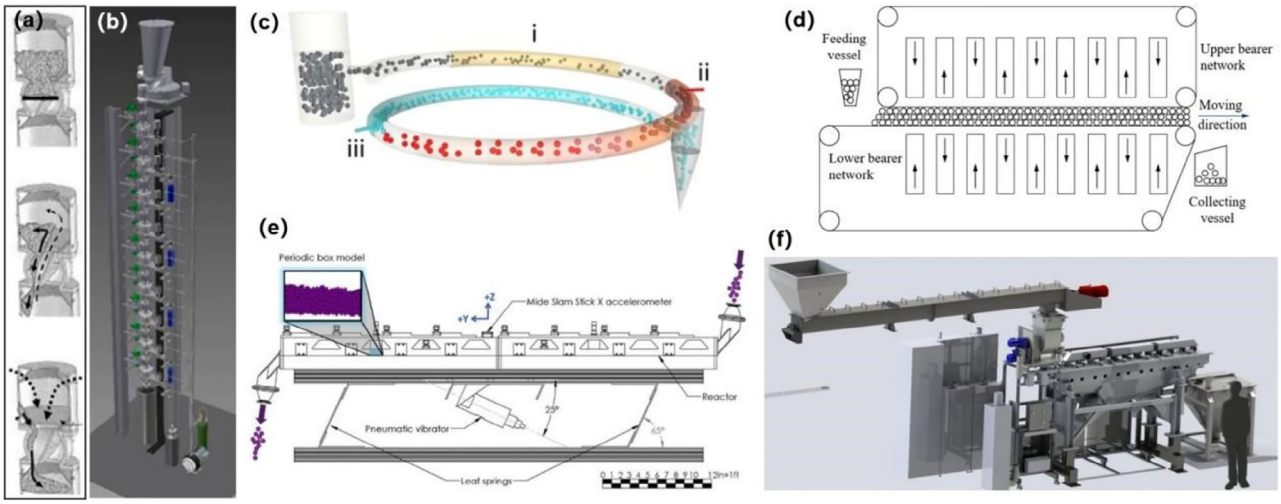

Figure 12. Designs of s-ALD reactors. a,b) Schematic diagram of a gravity-induced progressive ALD reactor with vertically placed powder reservoirs. Reproduced from the patent.[109] c) A pneumatic transport line reactor consisting preheating zone (i), reactant reaction zone (ii), and co-reactant reaction zone (iii). Reproduced with permission.[110] Copyright 2015, American Vacuum Society. d) Schematic diagram of a s-ALD reactor with the conveying belt to transport particles. Reproduced from the patent.[111] e) Setup of a continuously vibrating spatial PALD. Reproduced with permission.[113] Copyright 2021, Elsevier. f) Effect drawing of a vibration s-ALD system named as CIRCE by Forge Nano. Reproduced with permission.[92] Copyright 2023, Elsevier.

ferent zones, Chen et al. proposed to use a mechanical conveying belt to transport the particles which were located between two porous belts (Figure 12d).[111] In their design, the dispersion of particles and gas-particle interactions relied on the gas flow from the porous belts. With the particles moving to different reactant zones, the ALD reactions on the particle surfaces will be completed. It is noted that the operating pressure of the substrate is under atmospheric pressure. Similarly, A US patent also filed to apply the mechanical conveying belt to drive the particles to pass through different reactant and purging zones under atmospheric pressure.[112] In another design, the continuous s-ALD reactor could be developed based on the vibration.[113] As illustrated in Figure 12e, a pneumatic vibrator was employed to disperse the particles, thereby enhancing gas–particle and particle–particle interactions. Simultaneously, the vibration force drove the particles flow through alternating zones connected to the feeding vessel and collecting vessel. In the vibration continuous s-ALD reactor, the layering phenomenon of particles with a wide range of size distribution should be taken into account. According to the concept of Figure 12e, Forge Nano announced a continuous s-ALD system, named as CIRCE (Figure 12f), which can be operated at atmospheric pressure with a particle processing ability of maximum 4000 kg · h^{-1}.[114]

4.7. Comparison of t-ALD and s-ALD Reactors

Based on the above review of reactor designs, **Table 2** summarizes the characteristics of different ALD reactors. Fixed-bed reactors are used to clarify the possibility in coating micro-sized particles using the conventional and flat ALD system. These reactors suit for a small volume of particles, require long processing times and have low reactant utilization efficiency because of the poor gas–solid interactions. To overcome the drawbacks of fixed-bed reactors, some reactors, such as FBRs, rotating bed reactors and vibrating bed reactors, have been developed accordingly. By combining fluidization and ALD techniques, the FBR-ALD shows the ability in modifying the fine/ultra-fine particles and even NPs. Meanwhile, the FBRs have the potentials of scale-up for batch processing of particles. In FBRs, individual particles are not the fluidized entities but the particle agglomerates. The surfaces of individual particles can be modified in FBR-ALD due to the dynamic aggregation of particle agglomerates. The dynamic aggregation results from the shear forces exerted by the fluidizing gas and the collisions between the recirculating agglomerates. Usually, to improve the fluidization quality of particles, external mechanical forces, such as vibration, stirring and rotating, can be applied appropriately in the PALD system. However, in FBRs, the continuous fluidizing gas is needed to sustain the fluidized states of particles which may increase the consumption of the inert gas. Moreover, the fluidization parameters vary from different particle beds, and thereby switching between different particle beds is not straightforward. Although the pulsed-bed ALD reactor allows easy switching between different particle beds, it is convenient for processing very small quantity of particles.

Regarding the ALD surface reactions with low sticking coefficients, the residence time of reactant gases in the FBR may be too short to obtain high utilization efficiency of reactants. In this respect, the rotating bed reactor provides mechanical agitation along with the static exposure to ensure the sufficient interaction time between reactant gases and particle surfaces. In the rotating bed reactor, the particles are first lifted by the low speed of the rotating motion and then fall down from the reactor walls because that the centrifugal force induced by rotating motion of the reactor is lower than the gravitational force. Consequently, the soft agglomerates of fine/ultrafine particles will be disintegrated under the mechanical agitation. Rotating bed rectors can be applied to process particles with the wide size range from nanometers to millimeters. However, the scheme of breaking the soft agglomerates in rotating bed reactors may lead to the poor dispersion

Table 2. Comparison of t-ALD reactors.

Reactor type	Characteristics	Pros	Cons
Fixed-bed reactors	Static stacking of particles Reactants diffuse from the top layer to the bottom layer of the particle bed	Simple design Compatible to flat ALD reactors	Fitting for only small quantity of particles (several grams) Very long process time Low reactant utilization efficiency
Fluidized bed reactors	Particles keep at fluidized state due to balanced forces Fluidizing entities are particle agglomerates not individual particles Dynamic aggregation behavior of particles Intense solid recirculation of soft agglomerates and constant gas–solid contacts	Ability in coating films on individual particles Having the scale-up potential Usually being assisted by external mechanical methods (i.e., vibration, stirring, rotating, pulsation, etc.) to improve the fluidization quality	Large consumption of the fluidizing gas Appropriate for the particles that can be fluidized Fluidizing parameters vary from different particle beds, including bed mass, particle size, agglomerate kinetics, etc.
Rotating bed reactors	Applying rotation motion to mechanically break the soft agglomerates	Compatible to the particles with the wide size range from nanometers to millimeters Having the scale-up potential Static exposure to ensure sufficient interactions between reactants and surfaces	Poor dispersion of particles Long process time
Vibrating bed reactors	Introducing the vibration force to disperse the particles	Compatible to the particles with the wide size range from nanometers to millimeters	Layering phenomenon occurred in the particles with the wide range of size distribution Dispersion affected by the thickness of the particle bed Vibration adsorption to be needed for pipe joints

of particles and thereby the exposure times of reactants need to be prolonged in the PALD process. Furthermore, reactant gases flowing axially along the reactor's longitudinal direction could bypass the particle bed and thereby gases flowing radially along the reactor is expected to enhance the gas-solid interactions between particles and reactants.

In the vibrating bed reactor, the vibration force is introduced to disperse the particles and thereby enables the gas–solid interactions during the PALD process. The vibration forces and frequencies depend on the properties of substrate particles. Normally, the vibrating bed reactors are deemed to be compatible to the particles with wide size range from nanometers to millimeters. However, the layering phenomenon may occur in the particle beds, resulting in poor gas–solid interactions. Also, the thickness of particle bed affects the dispersion quality. Usually, the particles with thinner thickness is easier to be dispersed in the vibration bed. In the practical use, the vibration adsorption for pipe joints should be considered seriously in the vibrating bed ALD system. Otherwise the tightness of pipelines could be deteriorated as well as the ALD surface reactions.

The aforementioned PALD reactors belong to t-ALD reactors. Since that the quantity of particles to be processed is usually small at the lab-scale experiments, the fixed-bed reactors and pulse-bed reactors suit for the research purposes. When it comes to the mass production, the reactors are needed to be improved to process high-throughput particles. Some t-ALD reactors, such as FBRs and rotating bed reactors, have the scale-up potential. Via increasing the reactor volume, it was reported that the FBR with the particle capacity of kg-scale and rotating bed reactor with the ability in processing 100–1000 kg/batch particles have been successfully designed and manufactured for batch processing of particles. In the batch processing of particles, the reactor needs to be frequently disassembled and assembled. In this respect, s-ALD, designed for the continuous processing of particles, can drastically reduce the frequency of reactor disassembly and assembly. The main characteristics of continuous s-ALD, such as gravity-induced progressive ALD, vibration bed-based s-ALD, and pneumatic transport ALD, are summarized in **Table 3**.

In the gravity-induced s-ALD reactor, particles are forced to progressively flow through different reactant zones under the gravitational force to complete the half-reactions and purging steps in the ALD process. To make the particles flow through different reactant zones, the reactor should be installed vertically to take the most advantage of the gravity. It indicates that more ALD cycles mean more reactant zones as well as greater height of s-ALD reactors. Hence, this type of semi-continuous s-ALD reactors is considered to be suitable for low-cycle ALD processes, typically fewer than 10 cycles. Moreover, the dispersion of particles should be improved when large batch of particles is needed to be processed. In the vibration bed-based s-ALD reactors, the vibration forces are provided to disperse the particles and the particles flow through different reactant zones via mechanical conveying belts while the inert gas curtains can be applied to separate the different reactant zones. In this design, the influence of the vibration force on the pipe joints needs to be considered carefully. In the design of Chen et al., the particle dispersion and

Table 3. Comparison of s-ALD reactors.

Reactor type	Characteristics	Pros	Cons
Gravity-induced s-ALD reactors	Particles progressively flow through different reactant zones assisted by the gravity	Semi-continuous processing of particles Having full ALD reaction steps	Dispersion of particles needs to be improved More ALD cycles indicate taller height of reactors
Vibration bed-based s-ALD reactors	Particles disperse assisted by the vibration force, and flow through different reactant zones assisted by the vibration force	Continuous processing of particles Having full ALD reaction steps Operating at atmospheric pressure	Layering phenomenon of particles Limited thickness of particle bed for good dispersion Inert gas curtains required to separate different reactant zones
Mechanical conveying belt-based s-ALD reactors	Particles disperse by gas impact from the upper and lower porous belts, and flow through different reactant zones via a mechanical conveying belt	Continuous processing of particles Operating at atmospheric pressure	Dispersion of particles can be improved Thickness of particle bed may be small
Pneumatic transport s-ALD reactors	Particles spatially flow through different reactant zones via pneumatic transporting	Continuous processing of particles Good dispersion of particles Operating at atmospheric pressure	Breaking the integrity of ALD reaction steps, inducing granular films on particle surfaces Long length of reactors Large consumption of transporting gas

gas-particle interactions rely on the gas flow through the pores of mechanical conveyor belts. The s-ALD reactor processes particles continuously at atmospheric pressure, while the thickness of the particle bed may be small to ensure enough particle dispersion. Regarding the pneumatic transport s-ALD reactors at atmospheric pressure, the particles carried by the inert gas flow through the open tube comprised of different reactant zones via a pneumatic transportation. The pneumatic transportation can induce good dispersion of particles while large consumption of carrier gas is needed to maintain the transporting state of particles. Because that the purging steps are eliminated in the pneumatic transporting reactors, granular films on particle surfaces may take place. Another drawback of the pneumatic transporting s-ALD reactors lies in the length of reactors.

Overall, in order to process high-throughput particles, the designs of t-ALD reactors, such as rotating bed reactors, FBRs, etc., are expected to suit for batch processing of particles. As compared, the s-ALD reactors benefit continuous processing of particles. On the other hand, the continuous s-ALD reactors can be operated under atmospheric pressure, which results in drastic decrease of costs of the equipment and maintenance due to the free of the vacuum system and pipes in substrates. As a result, the atmospheric-pressure s-ALD reactors exhibit great advantages in the mass production. Therefore, to enable continuous processing of particles, spatially controlled ALD is preferred for mass production, although substantial efforts are needed to enhance the s-ALD apparatus through robust designs and cost-effectiveness.

5. Applications of ALD-Modified Particles

While efforts to design efficient reactors remain ongoing, advancements in PALD have significantly expanded the applicability of ALD-modified NPs. Normally, the ALD-coated films on particles can act as surface passivation layers, moisture diffusion barrier layers, and the like. Also, ALD technology can be used to decorate the particle surfaces with clusters for specific functions. Over the past decades, the researchers have attempted to apply PALD to explore the applications of ALD-modified NPs in various fields, such as energy, catalysis, luminescent, biomedicine, etc. In this section, the applications of modified functional (nano)particles using ALD will be concisely reviewed.

5.1. Energy

In the applications of batteries, active particulate materials in cathodes and anodes are easily destroyed by the side reactions of electrolytes. In this respect, ALD can deposit barrier layers to protect the active materials, effectively preventing the parasitic reactions between active cathode/anode materials and electrolytes. Cathode materials, such as high-nickel $LiNi_{0.8}Co_{0.1}Mn_{0.1}O_4$ (NCM811), were coated with ≈5 nm Al_2O_3 to alleviate the effects of side reactions between cathode materials and electrolytes in order to improve the cyclic performance.[115–117] Liang's group used Al_2O_3 ALD films to recover the degraded NCM811 particles. Their research results showed that Al_2O_3 ALD could remove the contaminant components (such as Li_2CO_3 and LiOH) of the particle surfaces exposed to moisture, inhibit side reactions during the charge and discharge process and enhance the cycling stability.[118] Further, Liang et al. employed Zr surface doping and Al coating as a synergetic method to modify NCM811 particles.[119] The results showed that Al_2O_3 ALD coating promoted the cyclic stability due to the improvement of surface chemistry of NCM811 particles, while Zr surface doping improved Li^+ transport properties and structural stability because that Zr doping expanded and supported the lattice structure of NCM811 particles.[119] As a result, the combination of Zr doping and Al coating improved the capacity retention after 200 cycles of charge/discharge (**Figure 13**a,b). In addition, this group coated ultrathin films of AlF_3 and Al_2O_3 on $Li_{1.2}Mn_{0.54}Co_{0.13}Ni_{0.13}O_2$ particles through FBR-ALD.[120] This AlF_3-Al_2O_3 coating could inhibit the decomposition of the electrolyte during the cyclic process to form the protective layers and thereby improved the Li ion

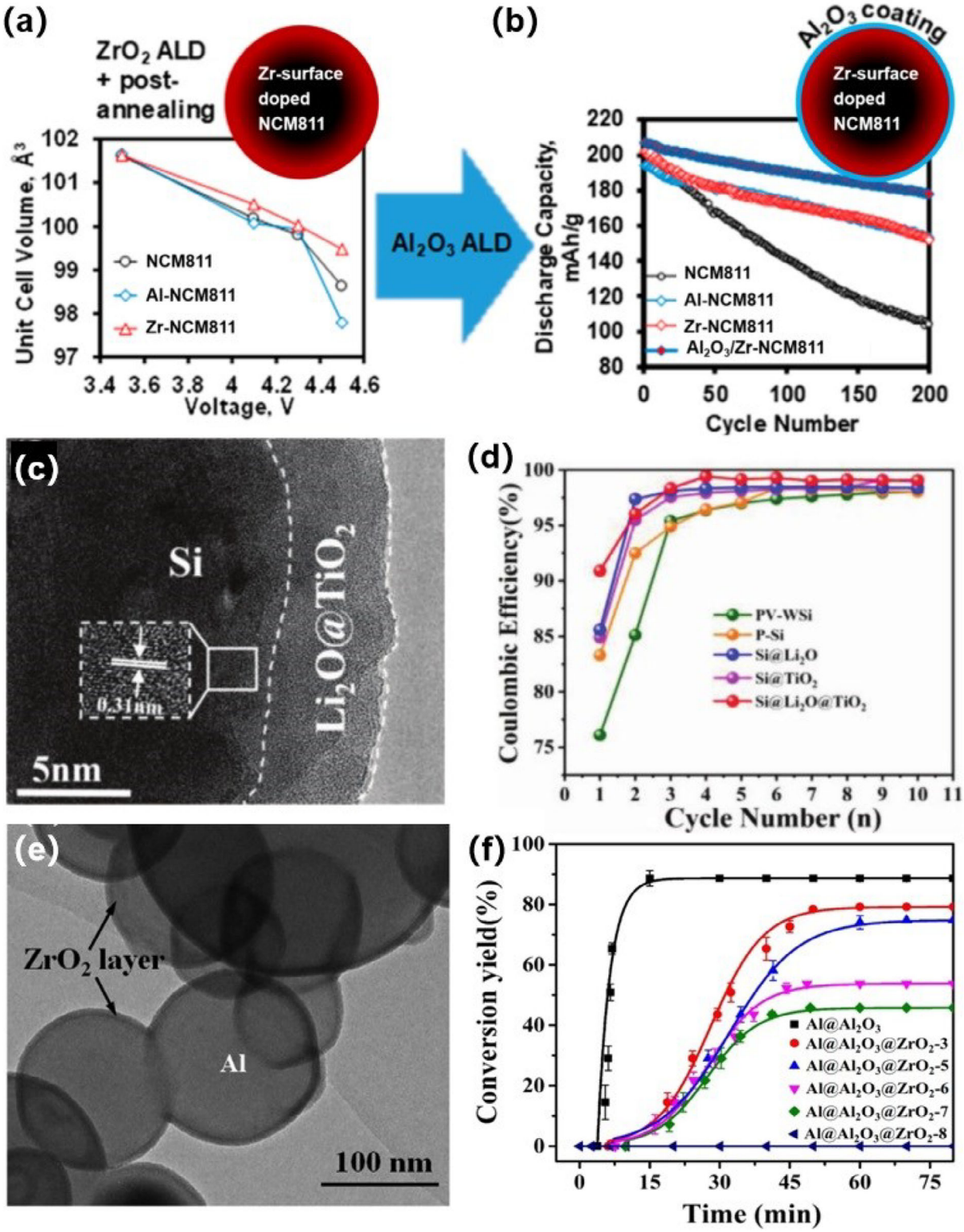

Figure 13. a) Unit cell volume of different particles (NCM811, Al-NCM811, and Zr-NCM811) after being charged to different volts. b) Discharge capacity curves after cyclic test for NCM811 particles with different treatments. Reproduced with permission.[119] Copyright 2020, American Chemical Society. c) TEM image of $Si@Li_2O@TiO_2$, and d) coulombic efficiency of different silicon anodes for the initial ten cycles. Reproduced with permission.[131] Copyright 2024, Wiley-VCH. e) Image of Al NPs modified with Al_2O_3 and ZrO_2 bilayers via ALD, and f) hydrogen conversion yield in water at 80 °C for Al NPs@Al_2O_3 and Al NPs@Al_2O_3@ZrO_2 as a function of ALD ZrO_2 cycles. Reproduced with permission.[136] Copyright 2018, American Chemical Society.

transport and cycling stability. Moreover, the repeatable electrochemical performance after storing over one year, indicated that the AlF_3-Al_2O_3 coating could provide protection for a long-term shelf life.[120] In the lithium-ion battery, it is commonly assumed that an optimally thin enough and uniform layer can protect the active materials while it do not hinder the mobility of ions between the cathode and anode materials. Compared to this supposition, Weimer's group first found that nonuniform and nonuniformly thick Al_2O_3 films appeared to improve the cycling stability of lithium-ion batteries.[121] In their study, less than 10 ALD cycles of Al_2O_3 were applied on NCM111 particles. It should be noted that the films deposited two to four cycles were not covering the substrate particles due to nucleation retardation in ALD. The results showed that initial deposition of Al_2O_3 preferentially covered the surface sites of transition metal oxides, remaining lithium-bound surface sites uncoated. This nonuniform surface coverage induced the exposure of some Li sites and thereby facilitated the movement of Li ions. Consequently, the stability of lithium-ion batteries had been improved by applying few-cycle Al_2O_3 ALD on NCM111 cathode materials.[121] The findings of preferential deposition are significantly important for the advanced engineering of cathode particle surfaces in the future.

Spinel $LiNi_{0.5}Mn_{1.5}O_4$ (LNMO) is also an attractive cathode material with the absence of cobalt elements due to its high operating voltages and energy density. With the ALD-coated ultrathin Al_2O_3 coating (<1 nm) on LNMO particles as a protective layer, the Al_2O_3-modified LNMO particles demonstrated suppressive dissolution of transition metals. Further investigations showed that the ALD-modified particulate material exhibited improvement of coulombic efficiency, cycle retention, rate capability, and suppression of self-discharge of transition metals.[122] It is noted that the above-mentioned cathode material particles coated at reduced pressures in PALD. Beetstra et al. demonstrated that the $LiMn_2O_4$ particles could be coated with Al_2O_3 conformal film under atmospheric pressure.[97] Although ALD has been explored as a reliable method to improve the performance of lithium-ion batteries, a trade-off between the species transport and protection induced by the insulating properties of ALD films is the key challenge. To address the problem, Patel et al. reported a breakthrough to overcome this trade-off by modifying the $LiMn_2O_4$ particle surfaces with conformal CeO_2 film as thin as about 3 nm.[123] With the ALD-coated CeO_2 nanoscale film, the particles demonstrated significant improvement of capacity and cycling performance due to the suppression of the impedance rise and the good electric conductivity of the CeO_2 film.[123]

In the solid oxide fuel cell (SOFC) area, highly active but unstable cathode materials, such as $La_{0.6}Sr_{0.4}CoO_{3-\delta}$ (LSCo) nanostructured electrodes, suffer from thermal instability and deteriorated catalytic activity in the intermediate temperature range (600–800 °C). Being coated with an ultrathin and conformal ZrO_2 layer, nanostructured LSCo particles could maintain long-term stability at 700 °C as well as retaining high oxygen reduction reaction (ORR) activity. The nanoscale ZrO_2 layer enabled the conduction of both electrons and oxide ions, suppression of the thermal growth of LSCo NPs and segregation of the surface strontium, resulting in the unique multifunctionality.[124] Similarly, Liang's group employed home-made PALD with a fluidized bed reactor to deposit ZrO_2 film as a stable interfacial layer to suppress the side reactions between electrodes and electrolytes, resulting in enhancement of the cycling stability of $Na_{0.7}MnO_2$ particles for sodium-ion batteries.[125] To suppress the side reactions in the all-solid-state electrolytes (ASSEs), Liang et al. deposited two ALD cycles of ZrO_2 on $LiFePO_4$ (LFP) particles to achieve the best electrochemical performance of LFP/ASSE/Li cell, because that ZrO_2 could stabilize the interface between cathodes and ASSEs.[126]

Due to the extremely high theoretical capacity of 4200 mAh g^{-1}, silicon has been considered one of the most promising anode materials for lithium-ion batteries despite that it faces challenges such as large volume expansion, etc.[127–129] Interface modification has been demonstrated as an effective method to suppress the silicon volume expansion. Fang et al. utilized molecular layer deposition (MLD) and ALD to deposit zincone and TiO_2 (≈5 nm) onto silicon NPs, respectively, thereby suppressing the silicon volume expansion.[130] They attributed the volume-expansion suppression to the buffer layer of the flexible nanoporous zincone.[130] Recently, Wang et al. utilized FBR-ALD to deposit Li_2O (≈1 nm) and TiO_2 (≈4 nm) onto photovoltaic silicon waste-based anode particles to form $Si@Li_2O@TiO_2$ structures (Figure 13c).[131] The layer of Li_2O served to compensate the loss of Li sources. And the amorphous TiO_2 layer could tolerate the large volume expansion of Si particles due to the elasticity and superior cushioning properties, and isolate the side reactions between Si and the electrolyte. Therefore, the prepared $Si@Li_2O@TiO_2$ demonstrated ultrahigh initial coulombic efficiency (90.9%), as shown in Figure 13d.

In lithium-ion batteries, the formation of lithium dendrites can deteriorate the electrochemical performance and induce safety issues. Although the lithium metal anode material have a theoretical capacity of 3860 mAh g^{-1}, the problem of dendrite formation hinders their commercialization. To suppress lithium dendrites, various strategies have been developed, such as electrolyte engineering, anode modification, etc.[132,133] ALD technique has proven to be effective in surface modification of electrolytes and anode materials. Kozen et al. demonstrated as a proof-of-concept that ALD of about 14 nm Al_2O_3 could protect the Li anode surface from the corrosion of atmosphere, sulfur, and electrolyte exposure.[134] In their study, the Li surface anode after 100 cycles showed that the density of the sulfur, carbon, and oxygen was significantly lower than that of the unprotected anode, suggesting that the protection of Al_2O_3 hindered the lithium dendrite formation upon cycling.[134] On the other hand, the low resistance of solid-state electrolytes (SSEs) hinders their applications in all-solid-state batteries, as the lithium-rich surfaces readily react with moisture and carbon dioxide in the atmospheric air to form lithium hydroxide (LiOH) and lithium carbonate (Li_2CO_3) on the surface. In addition, the relatively high electronic conductivity of the garnet-type SSE could cause lithium dendrite propagation due to formation of tunneling of electrons across the SSE. To modify the SSEs, Rajendran et al. utilized ALD to deposit ≈3-nm-thick h-BN with high chemical inertness onto the cleaned SSEs.[135] They attributed the effective suppression of lithium dendrites to the prevention of tunneling of electrons across the SSE and creation of a uniform lithium-ion flux caused by the inert ultrathin h-BN deposition. The prepared all-solid-state battery demonstrated long, stable cycling performance for over 100 cycles.[135]

Although aluminum (Al) NPs are attractive energetic materials in solid fuels, green propellants and fuel cells, the poor

stability of Al NPs hinders their applications. To enhance the stability of Al NPs, a common method is to coat a passivation layer, such as Al_2O_3, on the particles. However, Al_2O_3 film as a surface passivation layer cannot stabilize the Al NPs under hot water conditions, which is needed in preparing the slurry during the Al-based green propellant fabrication. Chen et al. developed a passivation method by utilizing ALD to coat an ultrathin ZrO_2 film on Al NPs (Figure 13e). After coating dual shells of Al_2O_3 and ZrO_2, the Al NPs@Al_2O_3@ZrO_2 nanoscale particles with 8 ALD cycles of ZrO_2 demonstrated nearly no hydrogen conversion yield (Figure 13f), indicating the good resistance in the water at 80 °C.[136] The authors attributed the performance enhancement of Al NPs to the structural stability and enhanced hydrophobicity toward water induced by the ZrO_2 film.

As discussed above, t-ALD reactors show wide applications in the energy field. S-ALD, including its atmospheric-pressure variant, has also demonstrated significant applications in energy storage systems.[137–139] For instance, Nguyen et al. applied atmospheric-pressure s-ALD to deposit phase pure 10 nm thick Cu_2O films as a hole-transporting layer in silicon solar cells with an area of 9 cm^2, obtaining a power conversion efficiency of 13.7%.[140] Li and co-workers utilized a rotary s-ALD reactor to prepare high-quality Al_2O_3 thin films for the edge passivation of tunnel-oxide passivated contact (TOPCon) half solar cells and they found that the combination of ALD Al_2O_3 for the edge passivation and annealing provided a great gain in the solar cell performance.[141] Recently, Anh et al. utilized s-ALD to deposit ZnO coatings onto Li-ion batteries. In their study, the slurry, consisting of NCM811 powders, conductive additives, and binders, was applied to an aluminum foil current collector using a doctor blade method. They demonstrated that depositing a 15-nm-thick amorphous ZnO coating on planar Ni-rich cathodes markedly improved the electrochemical performance and structural stability.[142] Although the substrates to be deposited in the s-ALD reactors were planar substrates not particles, this kind of s-ALD process offers a promising approach in the fields of batteries and photovoltaics.

5.2. Catalysis

ALD has also emerged as an interesting tool for the design and synthesis of catalytic materials.[4] Regarding the catalysts, there are four major aspects to evaluate their performance, including activity, selectivity, thermal stability, and durability. ALD has been utilized to improve the above-mentioned characteristics of catalysts.

To improve the durability and activity of Pt/C catalysts, McNeary et al. Deposited tungsten nitride (WN) and Pt nanostructures onto the functionalized carbon substrates to fabricate Pt/f-C catalysts via FBR-ALD.[143] First, Pt nanostructures were deposited on functionalized carbon black substrates to produce catalyst Pt/f-C. Then, 10 ALD cycles were used to deposit WN nanostructures on Pt/f-C substrates to form catalyst 10WN, and the catalyst 10WN was subjected to air oxidation followed by 725 °C reduction to produce 725 °C-10WN catalyst. As shown in **Figure 14a**, the WN nanostructures were homogeneously dispersed on the catalyst surface. Comparing the mass activity of the prepared catalysts, it was shown that the 725 °C-10WN catalyst had the best mass activity surpassing the benchmark Pt/C, ALD Pt/f-C, and 10WN catalysts.[143] Moreover, after 5000-cycle voltage cycling durability test, the mass activity also outperformed the other three catalysts (Figure 14b). The authors attributed the improvement of activity to the synergistic metal-support effects induced by W/WN nanostructures' proximity to Pt NPs and the enhancement of durability to the stabilizing effects of the W/WN structures.[143] To improve the activity of noble metal-based catalysts, Liu et al. deposited Pt NPs on Co_3O_4 nanotraps using ALD with a home-made FBR. The resulting Co_3O_4/Pt/Al_2O_3 catalyst exhibited outstanding room-temperature CO oxidation activity and thermal durability, retaining high catalytic activity even after calcination at 600 °C.[144] Hu et al. deposited Pt NPs on the surfaces of CeO_2 nanorods through ALD with a rotating FBR. The structure of the prepared catalyst with highly dispersed Pt NPs on CeO_2 nanorods decreased CO poisoning effect on Pt and activated oxygen around the interfaces, thereby improving the conversion of NO at a relatively low temperature of about 200 °C.[145] It was also reported that plasma-assisted fluidized bed ALD was utilized to deposit Pd-Cu bimetallic NPs on porous powders (a mixture of alumina, amorphous aluminum silicate, and molecular sieve), showing excellent catalytic performance for CO_2 hydrogenation.[146] Recently, Li et al. used atmospheric-pressure FBR-ALD to prepared Pt and Pd nanostructuring on carbon black supports to form Pt-Pd bimetallic electrocatalysts for CO_2 reduction to formic acid, and the results showed that the Pt-Pd alloy catalyst displayed a Faradaic efficiency of 46% toward formic acid, higher than those of Pt@Pd (22%) and Pd@Pt (11%) catalysts.[147]

As a widely used photocatalytic material, TiO_2 does not efficiently harvest the sunlight in the visible and infrared light regions. Moreover, the rapid recombination of photogenerated electrons and holes limits the high photocatalytic efficiency.[148] With the plasma-enhanced ALD, Co_3O_4-coated P25 TiO_2 NPs exhibited enhanced UV photocatalytic efficiency,[149] while TiO_xN_y-modified TiO_2 NPs showed highly visible light photocatalysis.[150] Using the atmospheric-pressure ALD, Benz et al. controlled the growth of ultrasmall Cu_2O clusters on P25 TiO_2 NPs, and the Cu_2O/TiO_2 catalysts exhibited enhanced photocatalytic activity.[151] To enhance the activity of oxygen evolution reaction (OER) of Cu-based electrocatalysts, Battiato et al. utilized atmospheric-pressure s-ALD to deposit Cu_2O thin film on silver nanowire (AgNW) networks at a deposition temperature of 200 °C using Cu(I)(hfac)(tmvs) and water as reactants.[152] The prepared AgNW@Cu_2O nanocomposites supported on cooper electrodes exhibited superior OER activity as compared to the bare copper substrate and bare AgNWs. They attributed the enhanced activity to the significantly large surface area and the active, accessible catalytic sites, both induced by Cu_2O coatings on AgNW with a three-dimensional network.[152] Besides enhancing the catalytic activity, the ALD modification can degrade the activity by blocking the reactive surfaces of catalytic NPs. The ultrathin Al_2O_3[153] and SiO_2[154] films had been conformally deposited on the TiO_2 NPs via vibration-assisted FBR or FBR, and the Al_2O_3-coated and SiO_2-coated TiO_2 NPs exhibited a degradation in photocatalytic performance. The Al_2O_3-coated TiO_2 with suppressed photocatalytic activity could be also prepared at room temperature and atmospheric pressure in the FBR-ALD.[155] Recently, Guo et al. tuned the photocatalytic activity of P25 TiO_2 NPs by depositing ultrathin SiO_2 films at the low temperature (100 °C)

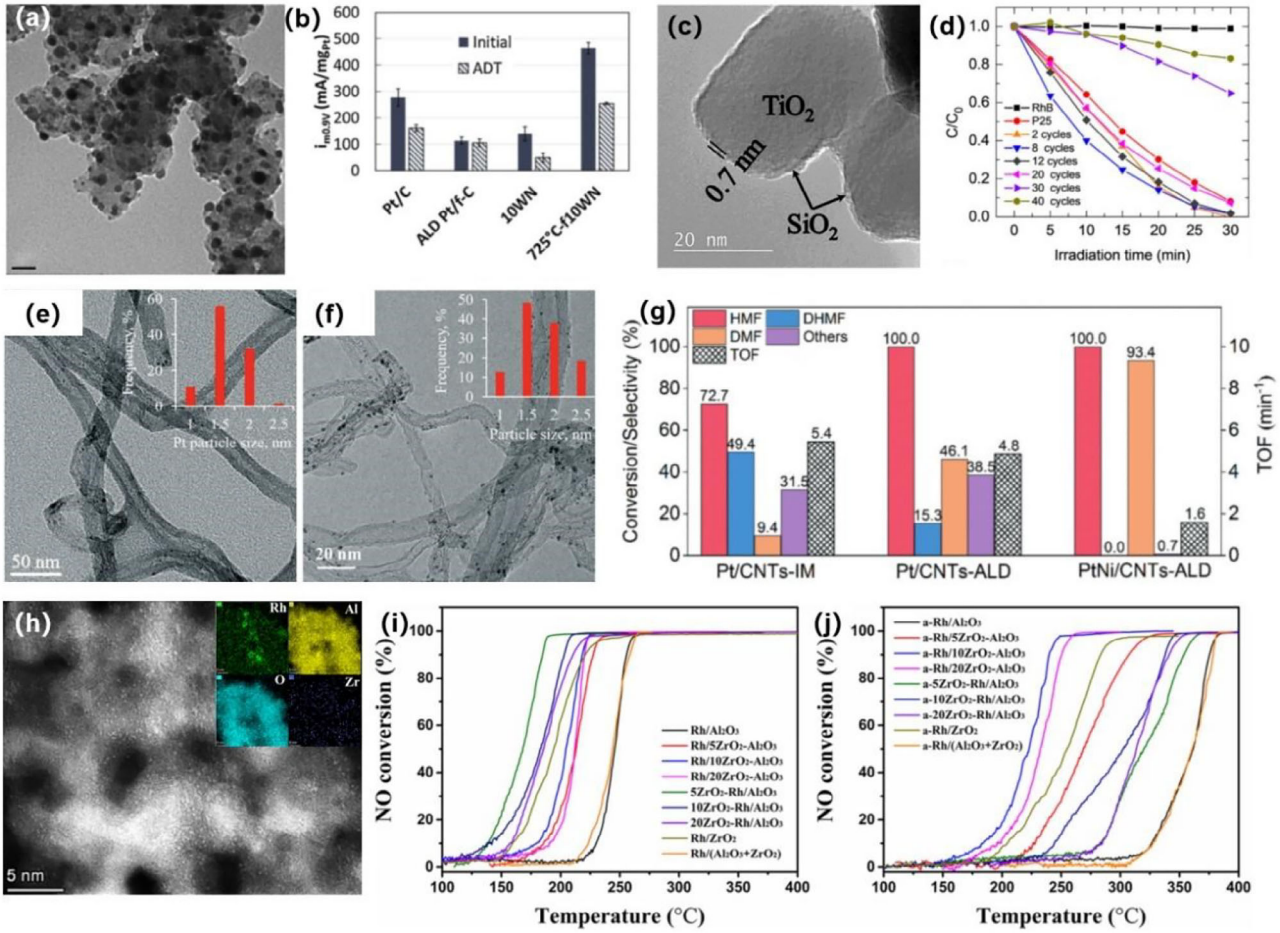

Figure 14. a) TEM image for ALD WN coated Pt/f-C catalysts after 725 °C treatment, and b) mass activities of the four catalysts initially and after a 5000-cycle voltage durability test. Reproduced with permission.[143] Copyright 2019, Elsevier. c) TEM image of TiO_2 NPs coated with SiO_2 films for 8 ALD cycles at the atmospheric pressure, and d) degradation of RhB as a function of irradiation time. Reproduced with permission.[156] Copyright 2020, Elsevier. e,f) TEM images of Pt/CNTs-ALD and PtNi/CNTs catalysts, and g) selective hydrogenation of HMF over the Pt-based catalysts prepared by different methods (Pt/CNTs-IM: simple impregnation method; Pt/CNTs-ALD and PtNi/CNTs-ALD: ALD method). Reproduced with permission.[157] Copyright 2021, The Royal Society of Chemistry. h) TEM image of the aged $Rh/10ZrO_2$-Al_2O_3 catalyst and the corresponding EDS mapping, and properties of NO conversion as a function of temperature i) before and j) after being aged at 1050 °C. Reproduced with permission.[164] Copyright 2022, American Chemical Society.

via the atmospheric-pressure ALD.[156] As shown in Figure 14c, after 8 ALD cycles, a conformal SiO_2 film with about 0.7 nm was coated on TiO_2 surfaces. The degradation properties of rhodamine B (RhB) under irradiation showed that the thickness of SiO_2 below 1.4 nm promoted the photocatalytic activity due to the improvement of charge separation induced by the Ti-O-Si bonds at the interface between TiO_2 and SiO_2, while the thickness of above 1.4 nm suppressed the photocatalytic activity due to the inhibition of the charge transport from TiO_2 to the outer surface (Figure 14d).

Selectivity is another important characteristic of Pt-based catalysts. Wang and co-workers compared the conversion and selectivity of carbon supported Pt catalysts prepared by impregnation and ALD methods.[157] In the 5-hydroxymethylfurfural (HMF) hydrogenation reaction, the main product was 2,5-bishydroxymethylfuran (DHMF) for the catalysts prepared by impregnation method, while the main product converted to 2,5-dimethylfuran (DMF) for the catalysts prepared by ALD methods, suggesting that the Pt-carbon interaction determined the reaction pathway. As shown in Figure 14e,f, Pt nanoclusters (Figure 14e) and PtNi nanoclusters (Figure 14f) were deposited on the multiwalled carbon nanotubes (CNTs) through ALD. Thanks to the synergistic effects between Pt and Ni NPs, the PtNi/CNTs-ALD bimetallic catalyst showed superior yield of DMF with complete HMF conversion (Figure 14g). It was noted that Pt ALD is commonly conducted at a temperature in the range of 200–300 °C.[157,158] However, a high temperature could induce the diffusion and coalescence of deposited Pt NPs, affecting the catalytic efficiency of Pt-based catalysts. To reduce the deposition temperature, some studies demonstrated that Pt NPs could be deposited on graphene nanoplatelets at 100 °C.[159,160] Recently, Van Bui and co-workers demonstrated that the deposition temperature of Pt NPs could be further lowered.[161] In their study, they utilized a home-built FBR-ALD, capable of operating at atmospheric pressure, to deposit Pt NPs at room temperature using $MeCpPtMe_3$ and O_2 as reactants. The results showed that highly dispersed Pt sub-nanometer clusters with an average cluster size of 0.6 nm were deposited on the surfaces of TiO_2 supports.[161]

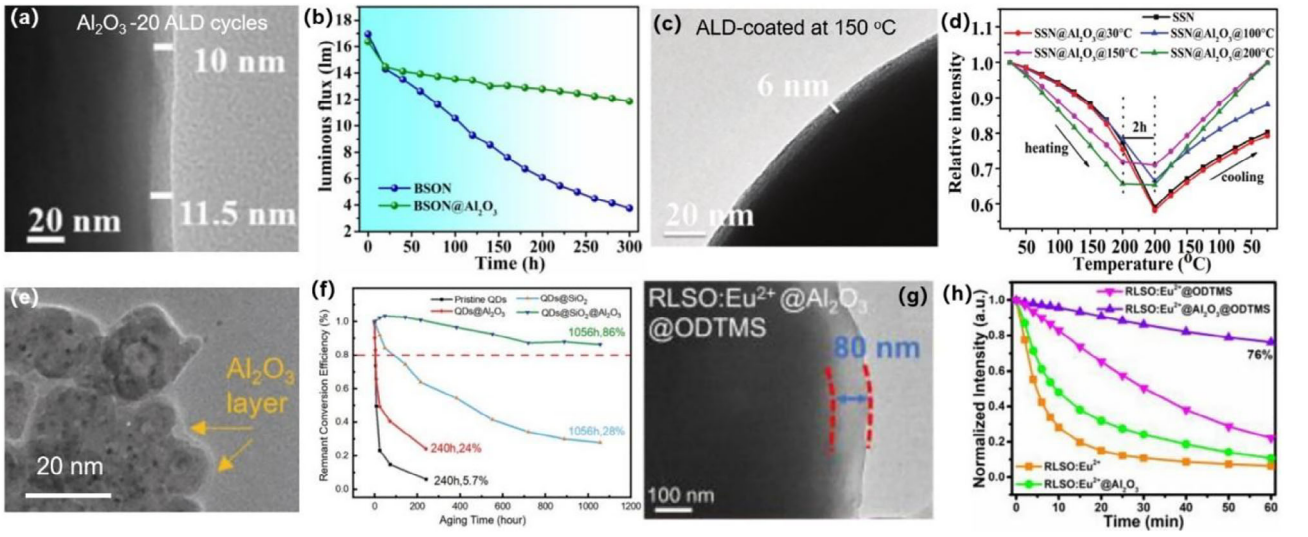

Figure 15. a) TEM image of $BaSi_2O_2N_2:Eu^{2+}$ (BSON) phosphor particle coated by Al_2O_3 nanofilm after 20 ALD cycles. b) Luminous flux properties of the uncoated and Al_2O_3-coated BSON phosphor particles as a function of aging time. Reproduced with permission.[165] Copyright 2024, Elsevier. c) TEM image of Al_2O_3-modified $Sr_2Si_5N_8$: Eu^{2+} (SSN) particle at ALD temperature of 150 °C. d) Temperature-dependent PL in air of SSN and SSN@Al_2O_3 at the different deposition temperatures. Reproduced with permission.[166] Copyright 2019, Royal Society of Chemistry. e) TEM image of CdZnSeS gradient alloyed QDs@SiO_2@Al_2O_3. f) Lifetime aging test of bare QDs, QDs@SiO_2, QDs@Al_2O_3, and QDs@SiO_2@Al_2O_3. Reproduced with permission.[170] Copyright 2020, Wiley-VCH. g) TEM image of RLSO:Eu^{2+}@Al_2O_3@ODTMS particle. h) Normalized PL intensities of RLSO:Eu^{2+}, RLSO:Eu^{2+}@Al_2O_3, RLSO:Eu^{2+}@ODTMS, and RLSO:Eu^{2+}@Al_2O_3@ODTMS immersed in water. Reproduced with permission.[171] Copyright 2020, Wiley-VCH.

To enhance the selectivity and durability of noble metal-based catalysts, MnO_x-decorated Pd/Al_2O_3 catalysts, fabricated via ALD with a rotating fluidized reactor, demonstrated high selectivity for benzyl alcohol oxidation along with remarkable catalytic yield.[162] Ni/Al_2O_3 catalysts, modified by ultrathin Co films using FBR-ALD, exhibited improved durability in the dry reforming of methane due to the highly active and coking resistance.[163]

In the field of exhaust gas treatments, Rh-based catalysts are considered appropriate catalysts for the reduction of NO_x due to their high activity. However, the Rh-based catalysts suffer aggregation of Rh NPs at high temperatures, leading to significant deactivation of the catalysts. To enhance the thermal stability, Guo et al. proposed to modulate the Rh active sites on the surfaces of Al_2O_3 nanorods via ALD method with a static bed reactor.[164] In their study, an ultralow number of ZrO_2 particles was initially deposited on Al_2O_3 supports using ALD technique to form ZrO_2-Al_2O_3 nanorods, and then Rh^{3+} was loaded on the nanorods through the wet impregnation method followed by calcination. Finally, the as-received fresh catalysts were treated at 1050 °C in air to obtain the aged catalysts.[164] Figure 14h shows the TEM image and corresponding EDS mapping of the aged Rh/ZrO_2-Al_2O_3 catalyst with 10 ALD cycles. The results display that the Rh remains highly dispersed on the Al_2O_3 nanorods support and ZrO_2 exists in the form of a granular film without an overcoating layer. With the fresh and aged catalysts, the catalytic performance of NO-CO reaction was investigated, as the results illustrated in Figure 14i,j. In Figure 14i, the T_{50} value of the fresh Rh/ZrO_2-Al_2O_3 catalyst with 5 ALD ZrO_2 cycles is lowered by about 76 °C compared to that of Rh/Al_2O_3. After heat treatment at 1050 °C, the T_{50} value of the ZrO_2 ALD-modified catalyst with 10 ALD cycles increases to about 220 °C, and that of aged Rh/Al_2O_3 climbs to about 360 °C, as illustrated in Figure 14j. It implies that the ZrO_2 ALD modification enhances the thermal stability of Rh-based catalysts under aging treatment at 1050 °C.

5.3. Luminescence

As a promising luminescent material used in white light-emitting diodes (wLEDs), cyan-emitting $BaSi_2O_2N_2:Eu^{2+}$ (BSON) phosphor particles suffer serious degradation under thermal attacks. To improve the thermal stability, Zhao et al. proposed to deposit nanosized Al_2O_3 films on the phosphor particles through FBR-ALD.[165] After 20 ALD cycles, the phosphor particles with the thickness of about 11 nm Al_2O_3 (**Figure 15a**) showed an increase in the oxidation temperature. Moreover, the wLEDs fabricated by Al_2O_3-coated phosphor particles remained 73% luminous flux of the initial value compared to the one of pristine particles which only remained 22% after aging for 300 h (Figure 15b). To reduce the thermal degradation of red-emitting $Sr_2Si_5N_8:Eu^{2+}$ (SSN:Eu^{2+}) phosphors, Zhao et al. proposed to modify the surface of phosphor particles with ultrathin Al_2O_3 films using vibration-assisted FBR which was operated at atmospheric pressure.[166] After 15 ALD cycles, the thickness of Al_2O_3 film at a deposition temperature of 150 °C was about 6 nm (Figure 15c). As the ALD deposition temperature increased, the thermal degradation of the coated samples decreased and it totally disappeared for the ALD-modified samples at 150 and 200 °C (Figure 15d). Further investigations of the thermalgravimetric analysis demonstrated that the Al_2O_3 coating increased the oxidation temperature of SSN phosphor from 700 to 850 °C, showing improved anti-oxidation behaviors.[166]

Due to the poor stability in humid and heat environments, the photoluminescence (PL) intensity of bare $CsPbBr_3$ quantum dots (QDs) can vanish in a very short time under the moisture condition. Although the scheme of embedding the QDs in silica sphere to form $CsPbBr_3$ QDs-silica luminescent sphere ($CsPbBr_3$ QDs-SLS) can avoid the contact with external environments and thereby improve the moisture resistance to some extent, the ligands of QDs may also get destroyed due to the embedding process which is based on hydrolysis or swelling process.[167,168] Xiang et al. utilized rotating fluidized ALD reactor to further modify the surfaces of $CsPbBr_3$ QDs-SLS with ultrathin Al_2O_3 films using TMA and H_2O as reactants.[169] Since that the surface of silica sphere was hydroxylated, TMA could easily react with the hydroxyl groups on silica surfaces and the surfaces of QDs, resulting in selective passivation of the unprotected sites of $CsPbBr_3$ QDs-SLS. As the alumina ALD cycles increase to 50, the coating film could effectively isolate the QDs-SLS from the external environment, showing almost unchanged PL intensity during ≈2 h under the water condition. The authors ascribed the enhancement of stability and retained PL quantum yield of the ALD-modified $CsPbBr_3$ QDs-SLS to the effective reduction of ion migration and crystal deformation induced by the nanosized Al_2O_3 coating.

The long term stability of QDs is a critical factor for the potential applications. To improve the stability, Fang et al. reported a novel encapsulation method by combining sol-gel method and ALD technique to form double shell configuration of QDs.[170] In their design, the employed QDs were CdZnSeS gradient alloyed QDs. The intermediate shell of SiO_2 was obtained by the hydrolysis of methoxysilane reactants in the QD solution. Then, they utilized ALD with a rotating FBR to obtain Al_2O_3 outer shell. After that, the ALD Al_2O_3 layer was coated on the QDs@SiO_2 particles (Figure 15e), subsequently forming QDs@SiO_2@Al_2O_3 luminescent microspheres (QLuMiS). The QDs@SiO_2 surface provided abundant hydroxyl species for the onset of ALD surface reactions during the deposition of Al_2O_3. And the water-oxygen channels in SiO_2 layer were blocked by the Al_2O_3 layer to improve the moisture resistance. In Figure 15f, the QDs@SiO_2@Al_2O_3 exhibits excellent stability with 86% of the initial light conversion efficiency after 1000 h of blue light aging, indicating improved long-term stability compared to QDs@SiO_2 and QDs@Al_2O_3 phosphors.[170]

Although $RbLi(Li_3SiO_4)_2:Eu^{2+}$ ($RLSO:Eu^{2+}$) phosphors possess excellent stability against thermal quenching, the poor chemical stability of phosphors hinder their further commercialization. To address the issue, Zhao et al. proposed a dual-shelled strategy to improve the moisture-resistant property of the humidity-sensitive phosphors. The dual-shelled protective $RLSO:Eu^{2+}$ phosphor particles were deposited with amorphous Al_2O_3 films via ALD and then the surface modification was carried out by using octadecyltrimethoxysilane (ODTMS) to form hydrophobic surfaces (Figure 15g).[171] In Figure 15h, it is seen that the pristine $RLSO:Eu^{2+}$ shows serious degradation trend than that of $RLSO:Eu^{2+}$@Al_2O_3 under the moisture condition. Moreover, the $RLSO:Eu^{2+}$ phosphor particles with dual protective shells of Al_2O_3 and ODTMS exhibited excellent moisture resistance performance compared to pristine and Al_2O_3-protected particles.[171]

5.4. Pharmaceutics and Biomedicine

Pharmaceutical particles, such as budesonide and lactose particles, are widely used in drug delivery and therapeutic applications. On the one hand, the therapeutics need to delivery pharmaceutical particles to the targeted sites in the body at a therapeutic concentration and for the required amount of time. It requires pharmaceutical particles to work at a controlled release manner. The surface modification of these particles can facilitate the controlled release system. On the other hand, these fine and organic particles are not only cohesive but also sensitive to humidity and temperature, leading to difficulty in dispersion and the need for specific conditions to modify their surfaces. Zhang et al. systematically investigated dispersion methods for fine inhalation-grade lactose powders (size range: 0.1–20 µm), which were designed specifically for dry powder inhalation (DPI).[44] The results of their study showed that the external force assisted fluidization method could fluidize the cohesive lactose particles, enabling the possibility of surface modification via ALD.[44] To obtain a controlled release system of drug particles, PALD technology was used to modify the surfaces of budesonide (d_{50} ≈ 1.76 µm) and lactose particles (d_{50} ≈ 3.53 µm). Zhang et al. utilized a vibration-assisted FBR to coat Al_2O_3 ultrathin films on the particles under near ambient conditions with 1 bar pressure and deposition temperature at no more than 40 °C.[6] The experimental results clearly demonstrated that the alumina layers were successfully coated on the lactose and budesonide particles, as shown in **Figure 16**a,b. With appropriate ALD cycles, the coated pharmaceutical particles can dissolute more slowly than the pristine particles (Figure 16c,d), leading to a controlled release manner. Moreover, Zhang et al. found that the surface of budesonide particles with Al_2O_3 nanosized films via atmospheric-pressure PALD enhanced the dissolution and extended release, which could benefit drug delivery applications.[172] In another study, La Zara et al. compared the wettability of budesonide particles coated by different ceramic coatings and methods. In their study, ceramic films (Al_2O_3, TiO_2, SiO_2) were prepared using atmospheric-pressure PALD, organic PET films using MLD and titanicone films using hybrid ALD/MLD method.[7] The results showed that the ceramic film-modified pharmaceutical particle surfaces exhibited high hydrophilicity (Figure 16e), while the titanicone film and PET film converted the budesonide particles into mild hydrophilicity and superhydrophobicity, respectively.[7] Furthermore, La Zara et al. used atmospheric-pressure FBR-ALD to coat nanoscale ceramic films to simultaneously tailor the release and aerosolization properties of inhaled budesonide particles without a lactose carrier, achieving controlled pulmonary delivery.[173] Recently, to improve the flow characteristics of inhaled budesonide powders, Zhang et al. deposited ceramic films on pharmaceutical particles by PALD to tailor the flow properties.[174] The results showed that the surface modification of budesonide particles enhanced the pulmonary delivery efficiency by significantly increasing the number of drug particles delivered, attributed to reduced interparticle forces between drug particles coated with inorganic nanofilms.[174]

Fe_3O_4 NPs have attracted great attention in biomedical applications, including magnetic resonance imaging, hyperthermia treatment, and targeted drug delivery. However, the Fe_3O_4 NPs

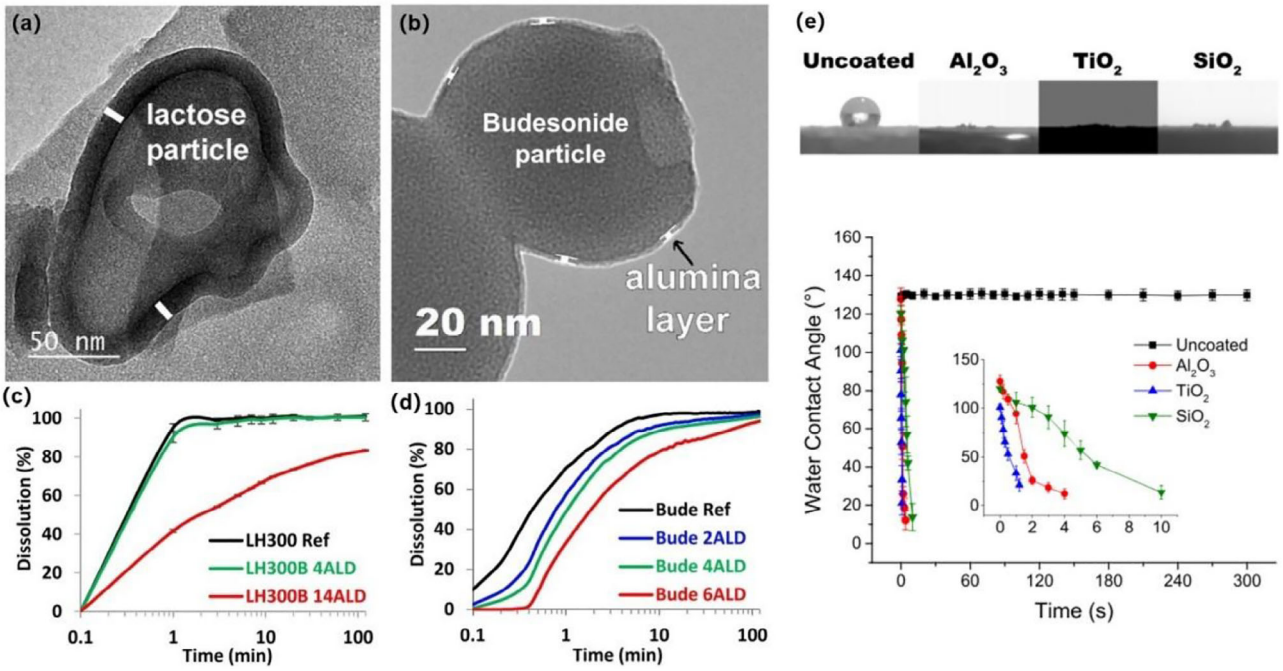

Figure 16. a) TEM image of Al_2O_3-modified lactose particles. b) TEM image of Al_2O_3-modified budesonide particles. c) Dissolution profiles of Al_2O_3-modified lactose particles and pristine particles. d) Dissolution profiles of Al_2O_3-modified budesonide particles and pristine particles. Reproduced with permission.[6] Copyright 2017, Royal Society of Chemistry. e) Wetting properties of ALD-modified budesonide particles. Reproduced with permission.[7] Copyright 2021, Elsevier.

suffer oxidation and magnetic loss under ambient conditions. Hence, the passivation of these NPs is usually required for practical applications. Duan et al. employed a home-built PALD system with a rotating FBR to deposit Al_2O_3 films on Fe_3O_4 NPs.[175] After 50 ALD cycles, an ultrathin and conformal Al_2O_3 film (≈5 nm) was successfully deposited on the Fe_3O_4 NPs. Moreover, the results of magnetic hysteresis loops of the pristine and Al_2O_3-coated Fe_3O_4 NPs showed that there existed little changes of saturation magnetization between the uncoated and coated particles, and the thermalgravimetric analysis demonstrated that the passivation of ultrathin Al_2O_3 could exhibit superior oxidation resistance, which is assumed to benefit the magnetic-based biomedical applications.

5.5. Cosmetics, Ceramics, and Others

PALD technology can be used as the surface modification of cosmetic particles. In cosmetic fields, ZnO and TiO_2 NPs have been frequently used for sunscreen products because of their excellent optical properties that allow absorption and scattering of ultraviolet (UV) lights. Normally, TiO_2 shows better protection of UVB (λ = 280–320 nm) lights, while ZnO has a broad absorption behaviors from UVA light (λ = 320–400 nm) to UVB light. When exposed to UV irradiation, the photoexcitation of TiO_2 NPs could induce the damage of human skin instead of protection. The commercial TiO_2-based sunscreen products, coated with organic materials to suppress the reaction with skin, suffer from the dissociation of organic materials due to the photocatalytic characteristic of TiO_2. To eliminate the phototoxicity of TiO_2 for the UV-protection application, Jang et al. proposed to coat ultrathin and conformal Al_2O_3 film on the surfaces of TiO_2 NPs using ALD technique.[176] With the introduction of ultrathin Al_2O_3 film (2–5 nm) on the surfaces of the particles, the absorption of UVA light by TiO_2@Al_2O_3 particles increased with Al_2O_3 film thickness. This improvement was attributed to the suppression of the photocatalytic activity of TiO_2 NPs. To utilize the characteristic of ZnO NPs in UVA absorption, King et al. demonstrated a drastic increase in the absorption for UVA light after depositing 10-nm ZnO film on the TiO_2 NPs using PALD with a FBR.[177]

Except for the above mentioned applications, PALD also shows promising potential uses in other fields. In the field of ceramics, Weimer's group deposited Al_2O_3 as a sintering aid on yttria-stabilized zirconia (YSZ) particles by PALD.[178–180] The results showed that the sintering temperature of YSZ was reduced by ≈75 °C after several PALD cycles of Al_2O_3 and that only one PALD cycle could drastically enhance the ion conductivity of YSZ ceramics, indicating promising scale-up potential.[178] As a promising material for electronic substrate and heat sinks, AlN particles suffer an adverse effect induced by the reaction between AlN particles and water. To mitigate the side effect, Weimer's group used PALD to coat Y_2O_3 conformal films on AlN particles before the densification and powder processing, revealing that the amorphous Y_2O_3 nanofilm with the thickness of about 6 nm could act as a barrier to suppress the hydrolysis reaction between AlN particles and aqueous solution, and thereby improved the relative density of AlN particles.[181] As for metallic particles, Cremers et al. applied ALD to deposit Al_2O_3 films (8–25 nm thickness) on Cu and Fe particles to enhance

the anti-oxidation properties.[182] And Liang's group used FBR-ALD to coat ceramic films (Al_2O_3, ZrO_2, HfO_2, and TiO_2) with less than 10 nm thickness in order to improve the corrosion resistance of Ag NPs.[183] Additionally, PALD can be used to coat ZrN films on low enriched uranium alloy particles as a diffusion barrier.[184]

6. Conclusion and Perspectives

PALD technology, which shows excellent ability in coating ultrathin and conformal films and decorating specific nanoclusters on almost any functional particles, has found wide applications in energy, catalysis, luminescence, human health, etc. With respect to the developments of PALD technology, the fundamentals of ALD, process conditions and challenges in particle dispersion have been discussed initially in the review. To hold and disperse NP substrates, t-ALD reactors with focusing on fixed-bed reactors, FBRs, rotating bed reactors and vibrating bed reactors have been reviewed. Some of these reactor designs, such as fixed-bed reactors and pulsed-bed reactors, are considered to be suitable for a small quantity of NPs, benefiting the research purposes. Some of the t-ALD reactors, such as FBRs and rotating bed reactors, can be utilized to process batch of NPs while they face the problems associated with the frequent disassembly and assembly of reactors. To this end, continuous processing of NPs is developed and the s-ALD reactors with focusing on gravity-induced s-ALD reactors, vibration bed-based s-ALD reactors and pneumatic transport s-ALD reactors have been introduced and discussed. Although great advancements on PALD reactors have been achieved over decades, there still exists some room for improvements.

In FBR, the individual particles are not the fluidized entities but the particle agglomerates, and dynamic aggregation of particles enables the ability in modifying the surface of individual particles. Since the size and geometry of particle agglomerates affect the fluidization behaviors, in-situ monitoring and characterization, such as in situ CCD camera systems and residual gas analyzers, are expected to be integrated into the FBR-ALD system for better reactant efficiency and film growth. In addition, compared to a single external force field, multiple external forces, such as mechanical stirring and vibration, might improve the fluidization quality and coating process in the FBR-ALD. Although most of the current FBR-ALD work under the reduced pressures, operation under atmospheric pressure is considered to be conductive to the mass production. In this case, the vapor pressures and introduction methods of reactant gases should be taken into account carefully. Regarding the design of rotating bed reactors, it can be used in batch production by simply manufacturing a large reaction chamber to hold a large number of particles, such as the equipment named LITHOS by Forge Nano. The major drawback may lie in the prolonged exposure time and purging time. Hence, the trade-off should be made between the particle batch and cost of process time in the rotating bed reactors. In addition, to avoid the reactant gases bypassing the particle bed, reactant gases are expected to flow radially through the reactors for enhancing better gas-solid interactions between gases and particles.

Continuous s-ALD reactors not only show great advantages in continuously processing a large quantity of particles but also can operate under atmospheric pressure or near atmospheric pressure which could lead to a reduction of the costs of equipment and maintenance. These s-ALD reactors are believed to be conducive to the industrial processing of particles. Besides the potential reduction of the cost, the cost of time, especially the purging time of the conventional ALD process, is required to be reduced in the scale-up solutions. In this respect, the s-ALD, which simultaneously doses reactants into the reactor and purges the exhaust gas, seems as a feasible strategy to decrease the cost of purging time, resulting enhancement of film deposition rate. Therefore, to design the s-ALD system operated at atmospheric pressure or near atmospheric pressure could be a tendency in the industrial sectors.

In ALD, there may exist initial nucleation difficulties that lead to non-continuous films in the initial coating. To obtain ultrathin and continuous films, one strategy is to combine ALD and thermal atomic layer etching (ALE). Recently, George's group utilized ALD (TDMAZ and H_2O as reactants) and ALE (HF and $TiCl_4$ as reactants) to control ZrO_2 thickness on TiO_2@ZrO_2 core@shell NPs in a rotary reactor, achieving ZrO_2 deposition rate of 0.09±0.01 nm per ALD cycle and etch rate of 0.65±0.02 nm per ALE cycle.[185] This work could open up a new field of research in particle ALD and ALE. On the other hand, designing of a FBR with superior gas–solid interactions compared to a rotary bed reactor could enable ALD and ALE in a single system. However, this approach requires careful considerations of anti-corrosion inner walls and integration of residual gas analyzers for precise control over particle deposition and etch processes.

With the surface modification to particles, PALD technology could show potentials in the field of rare earth magnets. In Nd-Fe-B magnet, to reduce the usage of heavy rare earth elements and noble elements, and enhance the coercivity of the magnets, one feasible strategy is to modify the grain boundary of the magnets. To this end, the eutectic alloys or powders with a low melting point, such as Cu- and Al-based compounds, have been reported to be added into the matrix phase to improve the wettability of grain boundary phase and demagnetization coupling effect, thereby improving the coercivity.[186,187] Similarly, Cu-based powders have been also employed in Sm-Co magnets to modify the microstructure of grain boundary areas, resulting in the improvement of magnetic properties.[188,189] Since that the Nd-Fe-B and Sm-Co magnets are fabricated from their precursor powders, it gives us a hint on decorating the surfaces of these magnetic precursor particles via ALD technique. Using ALD technique, the materials with the low melting point, such as Cu, Al and their compounds, can be deposited on the surfaces of magnetic precursor powders as ultrathin films or nanoclusters. Subsequently, in the heat treatment or hot pressing/deforming process, the deposited materials will be melted, transport uniformly around the precursor particles and modify the microstructure of grain boundary areas, which may improve the magnetic properties of the rare earth magnets. It should be noted that the content of oxygen, carbon and other non-friendly elements to the rare earth magnets are needed to be controlled strictly during the ALD process. Besides that, PALD will continue to expand into other areas, such as additive manufacturing. Via PALD, the materials with the low melting point can be deposited on the surfaces of metallurgical particles with a proper thickness before manufacturing process. Because that the deposited materials could form an ultrathin liquid layer around the metallurgical particles, the

rheological behaviors of particles could be enhanced during the manufacturing process, leading to improvement of some physical properties for the printed metallic parts. Overall, in the unfound or found application fields, PALD is a promising technology and can bring disruptive innovations in the future, although the further development of PALD reactors and economic process are needed to be improved.

Acknowledgements

This work was partially supported by the National Key Technologies R&D Program of China (No. 2021YFA0715302), the National Natural Science Foundation of China (Nos. 12475259 and 62375054), and the Science and Technology Commission of Shanghai Municipality (21142200200 and 22ZR1405000).

Conflict of Interest

The authors declare no conflict of interest.

Keywords

atmospheric pressure, atomic layer deposition, functional nanoparticle, spatial atomic layer deposition, surface modification

Received: February 14, 2025
Revised: May 29, 2025
Published online: July 4, 2025

[1] W. J. Stark, P. R. Stoessel, W. Wohlleben, A. Hafner, *Chem. Soc. Rev.* **2015**, *44*, 5793.
[2] J. R. van Ommen, J. M. Valverde, R. Pfeffer, *J. Nanopart. Res.* **2012**, *14*, 737.
[3] X. Meng, X. Q. Yang, X. Sun, *Adv. Mater.* **2012**, *24*, 3589.
[4] B. J. O'Neill, D. H. K. Jackson, J. Lee, C. Canlas, P. C. Stair, C. L. Marshall, J. W. Elam, T. F. Kuech, J. A. Dumesic, G. W. Huber, *ACS Catal.* **2015**, *5*, 1804.
[5] K. Cao, J. Cai, B. Shan, R. Chen, *Sci. Bull.* **2020**, *65*, 678.
[6] D. Zhang, M. J. Quayle, G. Petersson, J. R. van Ommen, S. Folestad, *Nanoscale* **2017**, *9*, 11410.
[7] D. La Zara, F. Zhang, F. Sun, M. R. Bailey, M. J. Quayle, G. Petersson, S. Folestad, J. R. van Ommen, *Appl. Mater. Today* **2021**, *22*, 100945.
[8] R. Chauhan, A. Kumar, R. Tripathi, A. Kumar, *Advancing of Zinc Oxide Nanoparticles for Cosmetic Applications, Handbook of Consumer Nanoproducts*, Springer, Berlin **2022**, p. 1057.
[9] R. M. Ahmed, I. Hasan, *Mater. Today Proc.* **2023**, *81*, 1073.
[10] S. L. Schneider, H. W. Lim, *Photodermatol. Photoimmunol. Photomed.* **2018**, *35*, 442.
[11] Z. Zhao, Y. Kong, Z. Zhang, G. Huang, Y. Mei, *J. Mater. Res.* **2019**, *35*, 701.
[12] S. Adhikari, S. Selvaraj, D. H. Kim, *Adv. Mater. Interfaces* **2018**, *5*, 1800581.
[13] J. R. van Ommen, A. Goulas, *Today Chem* **2019**, *14*, 100183.
[14] Y. Hu, J. Lu, H. Feng, *RSC Adv.* **2021**, *11*, 11918.
[15] Z. Li, J. Li, X. Liu, R. Chen, *Chem. Eng. Process.* **2021**, *159*, 108234.
[16] A. W. Weimer, *J. Nanopart. Res.* **2019**, *21*, 9.
[17] P. Dauthal, M. Mukhopadhyay, *Ind. Eng. Chem. Res.* **2016**, *55*, 9557.
[18] Y. Khan, H. Sadia, S. Z. Ali Shah, M. N. Khan, A. A. Shah, N. Ullah, M. F. Ullah, H. Bibi, O. T. Bafakeeh, N. B. Khedher, S. M. Eldin, B. M. Fadhl, M. I. Khan, *Catalysts* **2022**, *12*, 1386.
[19] K. A. Altammar, *Front. Microbiol.* **2023**, *14*, 1.
[20] H. Heinz, C. Pramanik, O. Heinz, Y. Ding, R. K. Mishra, D. Marchon, R. J. Flatt, I. Estrela-Lopis, J. Llop, S. Moya, R. F. Ziolo, *Surf. Sci. Rep.* **2017**, *72*, 1.
[21] K. Cao, J. Cai, X. Liu, R. Chen, *J. Vac. Sci. Technol., A* **2018**, *36*, 010801.
[22] M. Ahonen, M. Pessa, T. Suntola, *Thin Solid Films* **1980**, *65*, 301.
[23] S. M. George, A. W. Ott, J. W. Klaus, *J. Phys. Chem.* **1996**, *100*, 13121.
[24] S. M. George, *Chem. Rev.* **2010**, *110*, 111.
[25] J. P. K. Seville, C. D. Willett, P. C. Knight, *Powder Technol.* **2000**, *113*, 261.
[26] D. Longrie, D. Deduytsche, C. Detavernier, *J. Vac. Sci. Technol., A* **2014**, *32*, 010802.
[27] Y. Fan, L. Li, G. Yu, D. Geng, X. Zhang, W. Hu, *Adv. Mater.* **2020**, *33*, 2003956.
[28] J. W. Elam, D. Routkevitch, P. P. Mardilovich, S. M. George, *Chem. Mater.* **2003**, *15*, 3507.
[29] A. F. Palmstrom, P. K. Santra, S. F. Bent, *Nanoscale* **2015**, *7*, 12266.
[30] P. Poodt, D. C. Cameron, E. Dickey, S. M. George, V. Kuznetsov, G. N. Parsons, F. Roozeboom, G. Sundaram, A. Vermeer, *J. Vac. Sci. Technol., A* **2012**, *30*, 010802.
[31] D. Muñoz-Rojas, T. Maindron, A. Esteve, F. Piallat, J. C. S. Kools, J. M. Decams, *Mater. Today Chem.* **2019**, *12*, 96.
[32] P. Poodt, J. van Lieshout, A. Illiberi, R. Knaapen, F. Roozeboom, A. van Asten, *J. Vac. Sci. Technol., A* **2013**, *31*, 01A108.
[33] D. Muñoz-Rojas, V. Huong Nguyen, C. Masse de la Huerta, C. Jiménez, D. Bellet, *IntechOpen* **2019**, http://dx.doi.org/10.5772/intechopen.82439.
[34] R. Chen, S. F. Bent, *Adv. Mater.* **2006**, *18*, 1086.
[35] R. L. Puurunen, *J. Appl. Phys.* **2005**, *97*, 121301.
[36] M. Ritala, M. Leskelä, J.-P. Dekker, C. Mutsaers, P. J. Soininen, J. Skarp, *Chem. Vapor Depos.* **1999**, *5*, 7.
[37] R. L. Puurunen, *Chem. Vapor Depos.* **2003**, *9*, 249.
[38] R. L. Puurunen, W. Vandervorst, W. F. A. Besling, O. Richard, H. Bender, T. Conard, C. Zhao, A. Delabie, M. Caymax, S. De Gendt, M. Heyns, M. M. Viitanen, M. de Ridder, H. H. Brongersma, Y. Tamminga, T. Dao, T. de Win, M. Verheijen, M. Kaiser, M. Tuominen, *J. Appl. Phys.* **2004**, *96*, 4878.
[39] R. W. Johnson, A. Hultqvist, S. F. Bent, *Mater. Today* **2014**, *17*, 236.
[40] R. G. Gordon, D. Hausmann, E. Kim, J. Shepard, *Chem. Vapor Depos.* **2003**, *9*, 73.
[41] P. Poodt, A. Mameli, J. Schulpen, W. M. M. Kessels, F. Roozeboom, *J. Vac. Sci. Technol. A* **2017**, *35*, 021502.
[42] Y. Wang, G. S. Gu, F. Wei, J. Wu, *Powder Technol.* **2002**, *124*, 152.
[43] X. Zhu, Q. Zhang, Y. Wang, F. Wei, *Chin. J. Chem. Eng.* **2016**, *24*, 9.
[44] F. Zhang, D. La Zara, F. Sun, M. J. Quayle, G. Petersson, S. Folestad, J. R. van Ommen, *Can. J. Chem. Eng.* **2020**, *99*, 1696.
[45] C. Argeto, A. Jagota, W. C. Carter, *J. Mech. Phys. Solids* **1997**, *45*, 1161.
[46] X. Yang, Z. Ni, X. Yang, Q. He, H. Xie, X. Xu, Z. Xie, *Ceram. Int.* **2018**, *44*, 16459.
[47] Y. Liu, S. Lu, J. Luo, Y. Zhao, J. He, C. Liu, Z. Chen, X. Yu, *Polym. Adv. Technol.* **2023**, *34*, 1393.
[48] H. Sun, X. Liu, B. Liu, Z. Yin, *Mater. Res. Bull.* **2016**, *83*, 354.
[49] V. Torabinejad, M. Aliofkhazraei, S. Assareh, M. H. Allahyarzadeh, A. S. Rouhaghdam, *J. Alloys Compd.* **2017**, *691*, 841.
[50] A. Jaworek, A. T. Sobczyk, *J. Electrostat.* **2008**, *66*, 197.
[51] P. Fauchais, *J. Phys. D: Appl. Phys.* **2004**, *37*, R86.
[52] S. Qiao, Z. Shi, A. Tong, Y. Luo, Y. Zhang, M. Wang, Z. Huang, W. Xu, F. Chen, *Adv. Colloid Interface Sci.* **2025**, *341*, 103500.
[53] W. D. Kingery, H. K. Bowen, D. R. Uhlmann, *Introduction to Ceramics*, Wiley-VCH, Weinheim, Germany **1976**.
[54] Z. Zhao, D. Liu, J. Ma, X. Chen, *Chem. Eng. J.* **2020**, *388*, 124213.
[55] S. Kaliyaperumal, S. Barghi, J. Zhu, L. Briens, S. Rohani, *Powder Technol.* **2011**, *210*, 143.
[56] J. M. Valverde, A. Castellanos, *AIChE J.* **2006**, *52*, 1705.

[57] Q. Yu, R. N. Dave, C. Zhu, J. A. Quevedo, R. Pfeffer, *AIChE J.* **2005**, *51*, 1971.
[58] M. Kashyap, D. Gidaspow, M. Driscoll, *Powder Technol.* **2008**, *183*, 441.
[59] C. Zhu, G. Liu, Q. Yu, R. Pfeffer, R. N. Dave, C. H. Nam, *Powder Technol.* **2004**, *141*, 119.
[60] T. Keuter, N. H. Menzler, G. Mauer, F. Vondahlen, R. Vaßen, H. P. Buchkremer, *J. Vac. Sci. Technol., A* **2015**, *33*, 01A104.
[61] T. Onn, R. Küngas, P. Fornasiero, K. Huang, R. Gorte, *Inorganics* **2018**, *6*, 34.
[62] H. Van Bui, F. Grillo, J. R. van Ommen, *Chem. Commun.* **2017**, *53*, 45.
[63] V. Cremers, R. L. Puurunen, J. Dendooven, *Appl. Phys. Rev.* **2019**, *6*, 021302.
[64] D. M. King, J. A. Spencer, X. Liang, L. F. Hakim, A. W. Weimer, *Surf. Coat. Technol.* **2007**, *201*, 9163.
[65] F. Grillo, M. T. Kreutzer, J. R. van Ommen, *Chem. Eng. J.* **2015**, *268*, 384.
[66] J. D. Ferguson, W. Weimer, S. M. George, *Thin Solid Films* **2000**, *371*, 95.
[67] J. D. Ferguson, A. W. Weimer, S. M. George, *Appl. Surf. Sci.* **2000**, *162*, 280.
[68] J. R. Wank, S. M. George, A. W. Weimer, *J. Am. Ceram. Soc.* **2004**, *87*, 762.
[69] J. R. Wank, S. M. George, A. W. Weimer, *Powder Technol.* **2004**, *142*, 59.
[70] L. F. Hakim, S. M. George, A. W. Weimer, *Nanotechnology* **2005**, *16*, S375.
[71] L. F. Hakim, J. Blackson, S. M. George, A. W. Weimer, *Chem. Vapor Depos.* **2005**, *11*, 420.
[72] J. R. Grace, X. Bi, N. Ellis, *Essentials of Fluidization Technology*, Wiley-VCH, Weinheim, Germany **2020**.
[73] S. Ergun, *Chem. Eng. Prog.* **1952**, *48*, 89.
[74] M. Rhodes, *Introduction to Particle Technology*, 2nd ed., Wiley-VCH, Weinheim, Germany **2008**.
[75] R. D. Toomey, H. F. Johnstone, *Chem. Eng. Prog.* **1952**, *48*, 220.
[76] D. Geldart, *Powder Technol.* **1973**, *7*, 285.
[77] C. Zhu, Q. Yu, R. N. Dave, R. Pfeffer, *AIChE J.* **2005**, *51*, 426.
[78] D. Geldart, *Powder Technol.* **1978**, *19*, 133.
[79] J. M. Valverde, A. Castellanos, *Phys. Rev. E* **2007**, *75*, 031306.
[80] L. F. Hakim, J. L. Portman, M. D. Casper, A. W. Weimer, *Powder Technol.* **2005**, *160*, 149.
[81] M. Knudsen, *Ann. Phys.* **1909**, *333*, 75.
[82] J. F. O'Hanlon, T. A. Gessert, *A User's Guide to Vacuum Technology*, 4th ed., Wiley-VCH, Weinheim, Germany **2023**.
[83] C.-L. Duan, P.-H. Zhu, Z. Deng, Y. Li, B. Shan, H.-S. Fang, G. Feng, R. Chen, *J. Vac. Sci. Technol., A* **2017**, *35*, 01B102.
[84] J. Chaouki, C. Chavarie, D. Klvana, G. Pajonk, *Powder Technol.* **1985**, *43*, 117.
[85] S. Morooka, K. Kusakabe, A. Kobata, Y. Kato, *J. Chem. Eng. Jpn.* **1988**, *21*, 41.
[86] J. M. Valverde, A. Castellanos, *AIChE J.* **2005**, *52*, 838.
[87] Y. Iwadate, M. Horio, *Powder Technol.* **1998**, *100*, 223.
[88] R. E. Rosensweig, *Science* **1979**, *204*, 57.
[89] S. W. Park, J. W. Kim, H. J. Choi, J. H. Shim, *J. Vac. Sci. Technol., A* **2014**, *32*, 01A115.
[90] J. R. Wank, S. M. George, A. W. Weimer, *Powder Technol.* **2001**, *121*, 195.
[91] P. O. Oviroh, R. Akbarzadeh, D. Pan, R. A. M. Coetzee, T.-C. Jen, *Sci. Technol. Adv. Mater.* **2019**, *20*, 465.
[92] A. W. Weimer, *Powder Technol.* **2023**, *418*, 118279.
[93] A. P. Didden, J. Middelkoop, W. F. A. Besling, D. E. Nanu, R. van de Krol, *Rev. Sci. Instrum.* **2014**, *85*, 013905.
[94] M. Kobayashi, *Dissertation*, Northwestern University (Argonne) **1969**, p. 158.
[95] H. W. Wong, M. H. I. Baird, *Chem. Eng. J.* **1971**, *2*, 104.
[96] H. Tiznado, D. Domínguez, F. Muñoz-Muñoz, J. Romo-Herrera, R. Machorro, O. E. Contreras, G. Soto, *Powder Technol.* **2014**, *267*, 201.
[97] R. Beetstra, U. Lafont, J. Nijenhuis, E. M. Kelder, J. R. van Ommen, *Chem. Vapor Depos.* **2009**, *15*, 227.
[98] A. Goulas, J. R. van Ommen, *KONA Powder Part. J.* **2014**, *31*, 234.
[99] C. Soria-Hoyo, J. M. Valverde, J. R. van Ommen, P. E. Sánchez-Jiménez, L. A. Pérez-Maqueda, M. J. Sayagués, *Appl. Surf. Sci.* **2015**, *328*, 548.
[100] J. Dendooven, D. Deduytsche, J. Musschoot, R. L. Vanmeirhaeghe, C. Detavernier, *J. Electrochem. Soc.* **2009**, *156*, P63.
[101] J. A. McCormick, B. L. Cloutier, A. W. Weimer, S. M. George, *J. Vac. Sci. Technol., A* **2007**, *25*, 67.
[102] J. A. McCormick, K. P. Rice, D. F. Paul, A. W. Weimer, S. M. George, *Chem. Vapor Depos.* **2007**, *13*, 491.
[103] D. Longrie, D. Deduytsche, J. Haemers, K. Driesen, C. Detavernier, *Surf. Coat. Technol.* **2012**, *213*, 183.
[104] S. Watano, Y. Imada, K. Hamada, Y. Wakamatsu, Y. Tanabe, R. N. Dave, R. Pfeffer, *Powder Technol.* **2003**, *131*, 250.
[105] H. Nakamura, S. Watano, *Powder Technol.* **2008**, *183*, 324.
[106] C.-L. Duan, X. Liu, B. Shan, R. Chen, *Rev. Sci. Instrum.* **2015**, *86*, 075101.
[107] J. W. Elam, J. A. Libera, M. J. Pellin, P. C. Stair, *Appl. Phys. Lett.* **2007**, *91*, 243105.
[108] P. Poodt, A. Lankhorst, F. Roozeboom, K. Spee, D. Maas, A. Vermeer, *Adv. Mater.* **2010**, *22*, 3564.
[109] D. M. King, A. W. Weimer, P. Lichty, *US 20110236575 A1*, **2011**.
[110] J. R. van Ommen, D. Kooijman, M. de Niet, M. Talebi, A. Goulas, *J. Vac. Sci. Technol., A* **2015**, *33*, 021513.
[111] R. Chen, J. W. Li, B. Shan, X. Liu, J. R. Xiang, H. C. Shao, *CN 2021108142424*, **2021**.
[112] J. A. Spencer, R. A. Hall, *US 20230416914 A1*, **2023**.
[113] J. Hartig, H. C. Howard, T. J. Stelmach, A. W. Weimer, *Powder Technol.* **2021**, *386*, 209.
[114] Forge Nano, CIRCE equipment, https://www.atomiclayerdeposition.com/products/forgenano-circe, **2024**.
[115] L. Wang, Q. Su, W. Shi, C. Wang, H. Li, Y. Wang, G. Du, M. Zhang, W. Zhao, S. Ding, B. Xu, *Electrochim. Acta* **2022**, *435*, 141411.
[116] R. S. Negi, S. P. Culver, M. Wiche, S. Ahmed, K. Volz, M. T. Elm, *Phys. Chem. Chem. Phys.* **2021**, *23*, 6725.
[117] H. V. Ramasamy, S. Sinha, J. Park, M. Gong, V. Aravindan, J. Heo, Y.-S. Lee, *J. Electrochem. Sci. Technol.* **2019**, *10*, 196.
[118] H. Yu, Y. Gao, J. Kirtley, G. Borgmeyer, X. He, X. Liang, *J. Electrochem. Soc.* **2022**, *169*, 050520.
[119] Y. Gao, J. Park, X. Liang, *ACS Appl. Energy Mater.* **2020**, *3*, 8978.
[120] H. Yu, X. He, X. Liang, *ACS Appl. Mater. Interfaces* **2022**, *14*, 3991.
[121] A. L. Hoskins, W. W. McNeary, S. L. Millican, T. A. Gossett, A. Lai, Y. Gao, X. Liang, C. B. Musgrave, A. W. Weimer, *ACS Appl. Nano Mater.* **2019**, *2*, 6989.
[122] J. W. Kim, D. H. Kim, D. Y. Oh, H. Lee, J. H. Kim, J. H. Lee, Y. S. Jung, *J. Power Sources* **2015**, *274*, 1254.
[123] R. L. Patel, H. Xie, J. Park, H. Y. Asl, A. Choudhury, X. Liang, *Adv. Mater. Interfaces* **2015**, *2*, 1500046.
[124] Y. Gong, D. Palacio, X. Song, R. L. Patel, X. Liang, X. Zhao, J. B. Goodenough, K. Huang, *Nano Lett.* **2013**, *13*, 4340.
[125] H. Yu, M. Walsh, X. Liang, *ACS Appl. Mater. Interfaces* **2021**, *13*, 54884.
[126] Y. Jin, H. Yu, X. He, X. Liang, *ACS Appl. Energy Mater.* **2021**, *5*, 760.
[127] H. Zhao, X. Bo, H. Xu, L. Wang, W. A. Daoud, X. He, *Energy Storage Mater.* **2024**, *72*, 103696.

[128] Z.-L. Xu, X. Liu, Y. Luo, L. Zhou, J.-K. Kim, *Prog. Mater. Sci.* **2017**, *90*, 1.
[129] L. Wang, J. Yu, S. Li, F. Xi, W. Ma, K. Wei, J. Lu, Z. Tong, B. Liu, B. Luo, *Energy Storage Mater.* **2024**, *66*, 103243.
[130] J. B. Fang, Y. Q. Cao, S. Z. Chang, F. R. Teng, D. Wu, A. D. Li, *Adv. Funct. Mater.* **2021**, *32*, 2109682.
[131] L. Wang, J. J. Lu, S. Y. Li, F. S. Xi, Z. Q. Tong, X. H. Chen, K. X. Wei, W. H. Ma, *Adv. Funct. Mater.* **2024**, *34*, 2403574.
[132] Z. Liang, M. S. Nafis, D. Rodriguez, C. Ban, *Acc. Chem. Res.* **2024**, *57*, 3102.
[133] S. Chen, C. Pan, Q. Wang, J. L. Luo, X. Z. Fu, *Adv. Funct. Mater.* **2024**, *34*, 2409812.
[134] A. C. Kozen, c.-F. Lin, A. J. Pearse, M. A. Schroeder, X. Han, L. Hu, S.-B. Lee, G. Rubloff, M. Noked, *ACS Nano* **2015**, *9*, 5884.
[135] S. Rajendran, A. Pilli, O. Omolere, J. Kelber, L. M. R. Arava, *Chem. Mater.* **2021**, *33*, 3401.
[136] R. Chen, K. Qu, J. Li, P. Zhu, C. Duan, J. Zhang, X. Li, X. Liu, Z. Yang, *ACS Appl. Nano Mater.* **2018**, *1*, 5500.
[137] D. Muñoz-Rojas, V. H. Nguyen, C. Masse de la Huerta, S. Aghazadehchors, C. Jiménez, D. Bellet, *C. R. Phys.* **2017**, *18*, 391.
[138] D. Muñoz-Rojas, J. MacManus-Driscoll, *Mater. Horiz.* **2014**, *1*, 314.
[139] M. Chen, M. P. Nijboer, A. Y. Kovalgin, A. Nijmeijer, F. Roozeboom, M. W. J. Luiten-Olieman, *Dalton Trans.* **2023**, *52*, 10254.
[140] V. S. Nguyen, A. Sekkat, D. Bellet, G. Chichignoud, A. Kaminski-Cachopo, D. Muñoz-Rojas, W. Favre, *J. Mater. Chem. A* **2021**, *9*, 15968.
[141] W. Li, R. Zhou, Y. Wang, Q. Su, J. Yang, M. Xi, Y. Liu, *Appl. Surf. Sci.* **2024**, *673*, 160835.
[142] V. T. Anh, H.-A. T. Vu, V. H. Nguyen, H. X. Nang, L. T. Do, V.-D. Dao, N. H. Vu, *Mater. Chem. Phys.* **2025**, *336*, 130544.
[143] W. W. McNeary, S. F. Zaccarine, A. Lai, A. E. Linico, S. Pylypenko, A. W. Weimer, *Appl. Catal., B* **2019**, *254*, 587.
[144] X. Liu, Q. Zhu, Y. Lang, K. Cao, S. Chu, B. Shan, R. Chen, *Angew. Chem., Int. Ed.* **2017**, *56*, 1648.
[145] Q. Hu, K. Cao, Y. Lang, R. Chen, S. Chu, L. Jia, J. Yue, B. Shan, *Catal. Sci. Technol.* **2019**, *9*, 2664.
[146] X. Tian, D. Wang, B. Ouyang, Q. Chen, Z. Liu, X. Wang, *Plasma Sources Sci. Technol.* **2023**, *32*, 045010.
[147] M. Li, S. Fu, S. Saedy, A. Rajendrakumar, F. D. Tichelaar, R. Kortlever, J. R. van Ommen, *ChemCatChem* **2022**, *14*, 202200949.
[148] B. Ohtani, *Catalysts* **2013**, *3*, 942.
[149] X.-R. Zhao, Y.-Q. Cao, J. Chen, L. Zhu, X. Qian, A.-D. Li, D. Wu, *Nanoscale Res. Lett.* **2017**, *12*, 497.
[150] Y.-Q. Cao, X.-R. Zhao, J. Chen, W. Zhang, M. Li, L. Zhu, X.-J. Zhang, D. Wu, A.-D. Li, *Sci. Rep.* **2018**, *8*, 12131.
[151] D. Benz, Y. N. T. Nguyen, T.-L. T. Le, T.-H. T. Le, V.-T. Le, J. R. van Ommen, H. V. Bui, *Nanotechnology* **2021**, *32*, 425601.
[152] S. Battiato, A. Sekkat, C. S. Velasquez, A. L. Pellegrino, D. Bellet, A. Terrasi, S. Mirabella, D. Muñoz-Rojas, *Nanoscale Adv.* **2024**, *6*, 4426.
[153] H. Azizpour, M. Talebi, F. D. Tichelaar, R. Sotudeh-Gharebagh, J. Guo, J. R. van Ommen, N. Mostoufi, *Appl. Surf. Sci.* **2017**, *426*, 480.
[154] X. Liang, K. S. Barrett, Y.-B. Jiang, A. W. Weimer, *ACS Appl. Mater. Interfaces* **2010**, *2*, 2248.
[155] J. Guo, H. Van Bui, D. Valdesueiro, S. Yuan, B. Liang, J. van Ommen, *Nanomaterials* **2018**, *8*, 61.
[156] J. Guo, D. Benz, T.-T. Doan Nguyen, P.-H. Nguyen, T.-L. T. Le, H.-H. Nguyen, D. La Zara, B. Liang, H. T. Hintzen, J. R. van Ommen, H. Van Bui, *Appl. Surf. Sci.* **2020**, *530*, 147244.
[157] X. Wang, C. Zhang, B. Jin, X. Liang, Q. Wang, Z. Zhao, Q. Li, *Catal. Sci. Technol.* **2021**, *11*, 1298.
[158] H.-B.-R. Lee, S. F. Bent, *Chem. Mater.* **2011**, *24*, 279.
[159] H. Van Bui, F. Grillo, S. S. Kulkarni, R. Bevaart, N. Van Thang, B. van der Linden, J. A. Moulijn, M. Makkee, M. T. Kreutzer, J. R. van Ommen, *Nanoscale* **2017**, *9*, 10802.
[160] F. Grillo, H. Van Bui, J. A. Moulijn, M. T. Kreutzer, J. R. van Ommen, *J. Phys. Chem. Lett.* **2017**, *8*, 975.
[161] H. Van Bui, A. P. Nguyen, M. D. Dang, T. D. Dinh, P. J. Kooyman, J. R. van Ommen, *Chem. Commun.* **2024**, *60*, 14045.
[162] J. Yang, K. Cao, M. Gong, B. Shan, R. Chen, *J. Catal.* **2020**, *386*, 60.
[163] K. Cao, M. Gong, J. Yang, J. Cai, S. Chu, Z. Chen, B. Shan, R. Chen, *J. Catal.* **2019**, *373*, 351.
[164] F. Guo, J. Li, Y. Zhang, X. Yang, *J. Phys. Chem. Lett.* **2022**, *13*, 8825.
[165] Y. Zhao, X. Wang, Q.-a. Li, X. Zhang, Y. Li, R.-J. Xie, J. R. van Ommen, H. T. Hintzen, *Ceram. Int.* **2023**, *49*, 27423.
[166] Y. Zhao, L. Yin, O. M. ten Kate, B. Dierre, R. Abellon, R.-J. Xie, J. R. van Ommen, H. T. Hintzen, *J. Mater. Chem. C* **2019**, *7*, 5772.
[167] C. Sun, Y. Zhang, C. Ruan, C. Yin, X. Wang, Y. Wang, W. W. Yu, *Adv. Mater.* **2016**, *28*, 10088.
[168] H. C. Wang, S. Y. Lin, A. C. Tang, B. P. Singh, H. C. Tong, C. Y. Chen, Y. C. Lee, T. L. Tsai, R. S. Liu, *Angew. Chem., Int. Ed.* **2016**, *55*, 7924.
[169] Q. Xiang, B. Zhou, K. Cao, Y. Wen, Y. Li, Z. Wang, C. Jiang, B. Shan, R. Chen, *Chem. Mater.* **2018**, *30*, 8486.
[170] F. Fang, M. Liu, W. Chen, H. Yang, Y. Liu, X. Li, J. Hao, B. Xu, D. Wu, K. Cao, W. Lei, P. Müller-Buschbaum, X. W. Sun, R. Chen, K. Wang, *Adv. Opt. Mater.* **2020**, 1902118.
[171] M. Zhao, K. Cao, M. Liu, J. Zhang, R. Chen, Q. Zhang, Z. Xia, *Angew. Chem., Int. Ed.* **2020**, *59*, 12938.
[172] D. Zhang, D. La Zara, M. J. Quayle, G. Petersson, J. R. van Ommen, S. Folestad, *ACS Appl. Bio Mater.* **2019**, *2*, 1518.
[173] D. La Zara, F. Sun, F. Zhang, F. Franek, K. Balogh Sivars, J. Horndahl, S. Bates, M. Brännström, P. Ewing, M. J. Quayle, G. Petersson, S. Folestad, J. R. van Ommen, *ACS Nano* **2021**, *15*, 6684.
[174] F. Zhang, K. Wu, D. La Zara, F. Sun, M. J. Quayle, G. Petersson, S. Folestad, J. W. Chew, J. R. van Ommen, *Chem. Eng. J.* **2023**, *462*, 142131.
[175] C.-L. Duan, Z. Deng, K. Cao, H.-F. Yin, B. Shan, R. Chen, *J. Vac. Sci. Technol., A* **2016**, *34*, 04C103.
[176] E. Jang, K. Sridharan, Y. M. Park, T. J. Park, *Chem. - Eur. J.* **2016**, *22*, 12022.
[177] D. M. King, X. Liang, C. S. Carney, L. F. Hakim, P. Li, A. W. Weimer, *Adv. Funct. Mater.* **2008**, *18*, 607.
[178] R. J. O'Toole, C. J. Bartel, M. U. Kodas, A. J. Horrell, S. Ricote, N. P. Sullivan, C. J. Gump, C. B. Musgrave, A. W. Weimer, *J. Am. Ceram. Soc.* **2018**, *102*, 2283.
[179] R. J. O'Toole, P. J. Buur, C. J. Gump, C. B. Musgrave, A. W. Weimer, *J. Am. Ceram. Soc.* **2020**, *103*, 4101.
[180] R. J. O'Toole, B. Yoon, C. J. Gump, R. Raj, A. W. Weimer, *J. Am. Ceram. Soc.* **2021**, *104*, 2472.
[181] R. J. O'Toole, C. Hill, P. J. Buur, C. J. Bartel, C. J. Gump, C. B. Musgrave, A. W. Weimer, *J. Am. Ceram. Soc.* **2022**, *105*, 3123.
[182] V. Cremers, G. Rampelberg, A. Barhoum, P. Walters, N. Claes, T. M. d. Oliveira, G. V. Assche, S. Bals, J. Dendooven, C. Detavernier, *Surf. Coat. Technol.* **2018**, *349*, 1032.
[183] Y. Gao, M. Walsh, X. Liang, *Appl. Surf. Sci.* **2020**, *532*, 147374.
[184] S. Bhattacharya, L. Jamison, D. N. Seidman, W. Mohamed, Y. Bei, M. J. Pellin, A. M. Yacout, *J. Nucl. Mater.* **2019**, *526*, 151770.
[185] J. D. Sempel, M.-L. Kaariainen, T. A. Colleran, A. M. Lifschitz, S. M. George, *J. Vac. Sci. Technol., A* **2024**, *42*, 052604.
[186] S. Luo, Y. Lu, Y. Zou, S. Zhong, Y. Wu, M. Yang, *J. Magn. Magn. Mater.* **2021**, *523*, 167620.
[187] Y. I. Lee, G. Y. Huang, C. W. Shih, W. C. Chang, H. W. Chang, J. S. You, *J. Magn. Magn. Mater.* **2017**, *439*, 1.
[188] G. H. Yan, Z. Liu, W. X. Xia, C. Y. Zhang, G. Q. Wang, R. J. Chen, D. Lee, J. P. Liu, A. R. Yan, *J. Alloys Compd.* **2019**, *785*, 429.
[189] Y. Q. Wang, M. Yue, D. Wu, D. T. Zhang, W. Q. Liu, H. G. Zhang, *Scripta Mater* **2018**, *146*, 231.

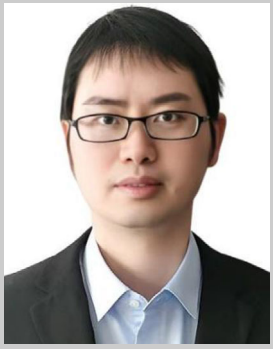

Guanghui Yan received his B.S. in materials physics from Wuhan University of Technology (China) and his M.S. and Ph.D. in materials physics and chemistry from Ningbo Institute of Materials Technology and Engineering, Chinese Academy of Sciences (China). Then, he completed his postdoctoral fellowship in the Department of Materials Science, Fudan University (China). Currently, he is an associate professor at Yiwu Research Institute of Fudan University (China). His research interest focuses on atomic layer deposition and magnetic materials.

Gaoshan Huang is a professor in International Institute of Intelligent Nanorobots and Nanosystems, Fudan University (China). He obtained his B.S. in physics and Ph.D. in condensed matter physics from Nanjing University (China). Then, he completed his postdoctoral fellowships at the Leibniz Institute for Solid State and Materials Research Dresden (Germany) and the Institute of Materials Research and Engineering (Singapore). His current research interests are smart materials, sensors, and micro-/nano-robotics.

Jianjun Shi is a professor at Yiwu Research Institute of Fudan University (China). He obtained his B.S. and M.S. from Nanjing University (China) and his Ph.D. from Loughborough University (UK). He completed his postdoctoral fellowship in the Department of Power Electronics Engineering, Loughborough University (UK). His current research interests are plasma-assisted atomic layer deposition and atmospheric-pressure plasma.

Yi Ouyang received his Ph.D. in materials physics and chemistry from the Ningbo Institute of Materials Technology and Engineering, Chinese Academy of Sciences (China). He completed his postdoctoral fellowship in the Department of Materials Science, Fudan University (China). Currently, he is an associate professor at Yiwu Research Institute of Fudan University (China). His research interest focuses on atomic layer etching and magnetic soft robots.

Yongfeng Mei received his B.S. and M.S. in physics from Nanjing University and his Ph.D. in materials physics from City University of Hong Kong (China). He is a professor in International Institute of Intelligent Nanorobots and Nanosystems and the deputy dean of graduate school at Fudan University (China). Before that, he worked as a postdoctoral researcher at the Max Planck Institute for Solid State Research (Germany) and then led a research group at the Leibniz Institute for Solid State and Materials Research Dresden (Germany) as a staff scientist. His research interest focuses on flexible electronics/optoelectronics, nanophotonics, and micro-/nano-robotics.